Satellite survey sheds new light on global solid waste methane emissions

Matthieu Dogniaux[1], Joannes D. Maasakkers[1], Marianne Girard[2], Dylan Jervis[2], Jason McKeever[2], Berend J. Schuit[1,2], Shubham Sharma[1], Ana Lopez-Noreña[1], Daniel J. Varon[3] and Ilse Aben[1]

[1]SRON Netherlands Institute for Space Research

[2]GHGSat, Inc.

[3]School of Engineering and Applied Sciences, Harvard University

Corresponding author: Matthieu Dogniaux
Corresponding author email: M.Dogniaux@sron.nl

This is a non-peer reviewed preprint submitted to EarthArXiv.

Satellite survey sheds new light on global solid waste methane emissions

Matthieu Dogniaux[1], Joannes D. Maasakkers[1], Marianne Girard[2], Dylan Jervis[2], Jason McKeever[2], Berend J. Schuit[1,2], Shubham Sharma[1], Ana Lopez-Noreña[1], Daniel J. Varon[3] and Ilse Aben[1]

[1]SRON Netherlands Institute for Space Research

[2]GHGSat, Inc.

[3]School of Engineering and Applied Sciences, Harvard University

Summary

Anthropogenic methane emissions are the second most important contributor to climate change[1], and their rapid reductions could help decrease near-term warming[2]. Solid waste emits methane through the decay of organic material, which amounts to about 10% of total anthropogenic methane emissions[3]. Satellite instruments[4] enable monitoring of strong methane hotspots[5], including many strongly emitting urban areas that include landfills as most prominent sources[6]. We present a survey of methane emissions from 151 individual waste disposal sites across six continents using high-resolution satellite observations. We find that managed landfills and dumping sites show similar levels of emission and our satellite-based estimates generally show no correlation with reported or modeled emission estimates. This reveals major uncertainties in the current understanding of methane

emissions from waste-disposal sites, warranting further investigations to reconcile bottom-up and top-down approaches. We also emphasize how high-resolution satellite observations can help pinpoint where emissions originate within a facility, which often aligns with the area where waste is added. Our results highlight the potential of high-resolution satellite observations to detect and monitor methane emissions from the waste sector globally, providing actionable insights to help improve emission estimates and focus mitigation efforts.

Body text

Global waste production has nearly tripled since 1965, reaching 2 billion tons per year in 2016 and, with growing urbanization and economic development, is expected to further increase by 70% by 2050[7]. Close to 70% of waste currently ends up in landfills or dumping sites[7], where anaerobic decomposition of organic material produces methane. Methane is a short-lived but potent greenhouse gas and its anthropogenic emissions are the second most important contributor to human-induced climate change, accounting for ~30% of current positive warming[1]. Deep and rapid reductions in global anthropogenic methane emissions are essential to keep warming below 1.5°C by 2100[2,8]. Currently, methane emissions from solid waste amount to 38 million tons per year, roughly 10% of total methane emissions[3], and could reach 60 million tons annually by 2050[9]. However, if separation of organic materials, treatment with energy recovery and bans on landfilling organic waste are implemented to their fullest potential, 2050 methane emissions from solid waste could be as low as 11 million tons per year[9].

These emission estimates are based on widely used first-order decay models[10] that are also used in country-level reporting of methane emissions[11] and employed at facility scale. Different variants of such models exist and can yield very different results for similar facilities[12]. The parameters (e.g. methane generation potential of the waste) that drive them are also uncertain and specific to each facility[13,14]. Finally, waste disposal management practices can impact methane emissions greatly, from unmanaged dumping sites to managed sanitary landfills that include linings, covers and gas capture systems of variable efficiency[15]. Considering all these uncertainties, independent observations of methane emitted from waste disposal sites are critical[16]. Here, we present a global-scale survey of methane emissions from waste disposal sites using close to 1500 high-resolution satellite observations.

Satellite remote sensing of atmospheric methane can play an active role in methane emission mitigation by locating emission hotspots and super-emitting point sources[17]. Over the last decade, a range of spaceborne instruments have been transformative for methane imaging from space[4,18–23]. These include the TROPOspheric Monitoring Instrument (TROPOMI) [24,25] on board of the Sentinel-5 Precursor satellite, which maps the atmospheric concentration of methane with daily global coverage and a resolution down to 7 x 5.5 km^2. Its observations have been successfully used to detect[5] and analyze emission plumes from oil & gas[26,27], coal mining[28,29], and urban areas[6,30]. The constellation of GHGSat's high-resolution (~25 x 25 m^2) methane imaging satellites can detect methane plumes down to 100 kg/hr from individual facilities including onshore[31] and offshore[32] oil and gas sites, coal mines[33] and landfills[6]. As GHGSat takes targeted 12 x 15 km^2 images, TROPOMI's global coverage has been key in providing targets for GHGSat to observe. This has been demonstrated for four urban areas with strongly-emitting landfills[6]. Here, we present a global GHGSat-based survey of methane emissions from waste disposal sites across 130 urban areas of 47 countries in 2021 and 2022, substantially guided by TROPOMI detections of urban emissions.

A third of 2021 methane emission plumes detected in TROPOMI data are related to urban areas[5]. In 2021 and 2022, we detect 897 plumes with TROPOMI across 46 urban areas among the 130 covered by GHGSat. Plumes are detected on six different continents, with the majority coming from Asia (Figure 1). These 46 urban areas (see examples in Figure 2) have a median plume emission rate of 19 t/hr (5^{th} and 95^{th} percentiles of 5 t/hr and 74 t/hr, respectively, see Methods and Supplements S1 and S2), illustrating the large magnitude of urban emissions (including all sectors). 14 urban areas have at least 21 detected plumes, encompassing 82% of all plume detections. Among considered urban areas that do not show TROPOMI-detected plumes, most of them are either hampered by coverage-related issues (e.g. persistent cloudiness or sharp elevation gradients, 62 areas) or are not expected to have total emissions exceeding the ~8 t/hr TROPOMI plume detection threshold[5], based on emission inventories[3] and GHGSat (19 areas, see Supplements S3). Plume-based estimates are not necessarily representative of mean urban emissions, as only large, concentrated plumes can be detected. However, they do show the mitigation potential concentrated in urban areas. Urban areas harbor a range of sources including wastewater treatment, natural gas distribution, and incomplete combustion[34]. Waste disposal sites, however, are the most concentrated and mitigatable sources and are therefore the facilities that we focus on in our GHGSat analysis.

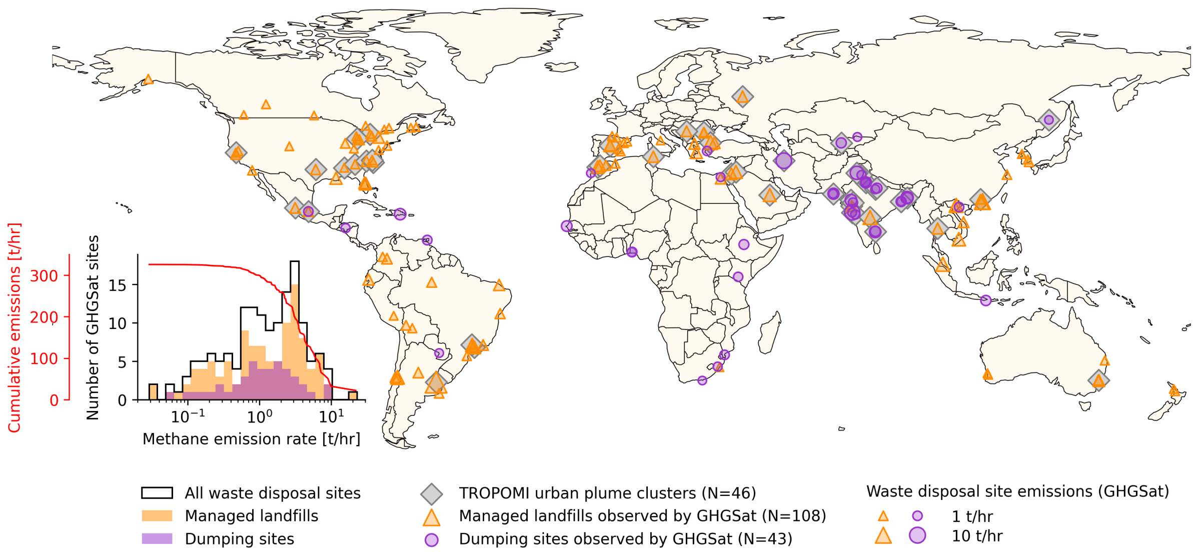

Figure 1. Location of the 151 waste-disposal sites observed by GHGSat satellites, and of the 46 out of 130 corresponding urban areas for which methane emission plumes have been detected in TROPOMI data (grey). GHGSat methane emission rate distributions over logarithmically-spaced bins are given for all sites (black line), and for managed landfills (orange) and dumping sites (purple) separately. The site-level and urban area-level data supporting this Figure are provided in the Supplements.

We use 1447 clear-sky observations acquired by GHGSat's C1-C5 satellites in 2021 and 2022. These were targeted at 151 different waste-disposal sites located in 130 urban areas scattered over six continents, as shown in Figure 1. Only sites for which at least one methane emission plume has been detected by GHGSat are included. The median number of GHGSat observations per site is 5, with 23 sites that have been observed at least 20 times (see Supplements S4). These are opportunistic observations that could be made in parallel to regular GHGSat activities, a substantial fraction (51%) of which intersect with TROPOMI-detected urban methane hotspots.

Out of the 1447 observations, 1085 show at least one emission plume above GHGSat's detection threshold (Examples are shown in Figure 2; quantified as described in Methods). We conservatively consider the emission rate of the 449 site-level null detections to be zero even though we may miss (diffuse or not) emissions that are lower than the GHGSat detection threshold. The positive plume detection rate per site ranges from 7% (2 plumes among 30 observations at Icheon, South Korea) to 100%, which we find for 74 sites. The plumes' detected methane emission rates show a 2.4 t/hr median with 5^{th} and 95^{th} percentiles of 0.5 t/hr and 15.4 t/hr, respectively.

Recurrent observations allow us to investigate the potential drivers of the detected emission variability. We compare site-wise emission variability against meteorology, including surface pressure change, but do not find any significant link between them (see Supplements S5). Although surface pressure change has been reported to drive landfill methane emissions in on-site studies[35–37], our findings based on satellite observations of high-emitting active sites are consistent with recent airborne-based results[38]. This finding suggests that operational practices could be driving emission variability for the sites we observed.

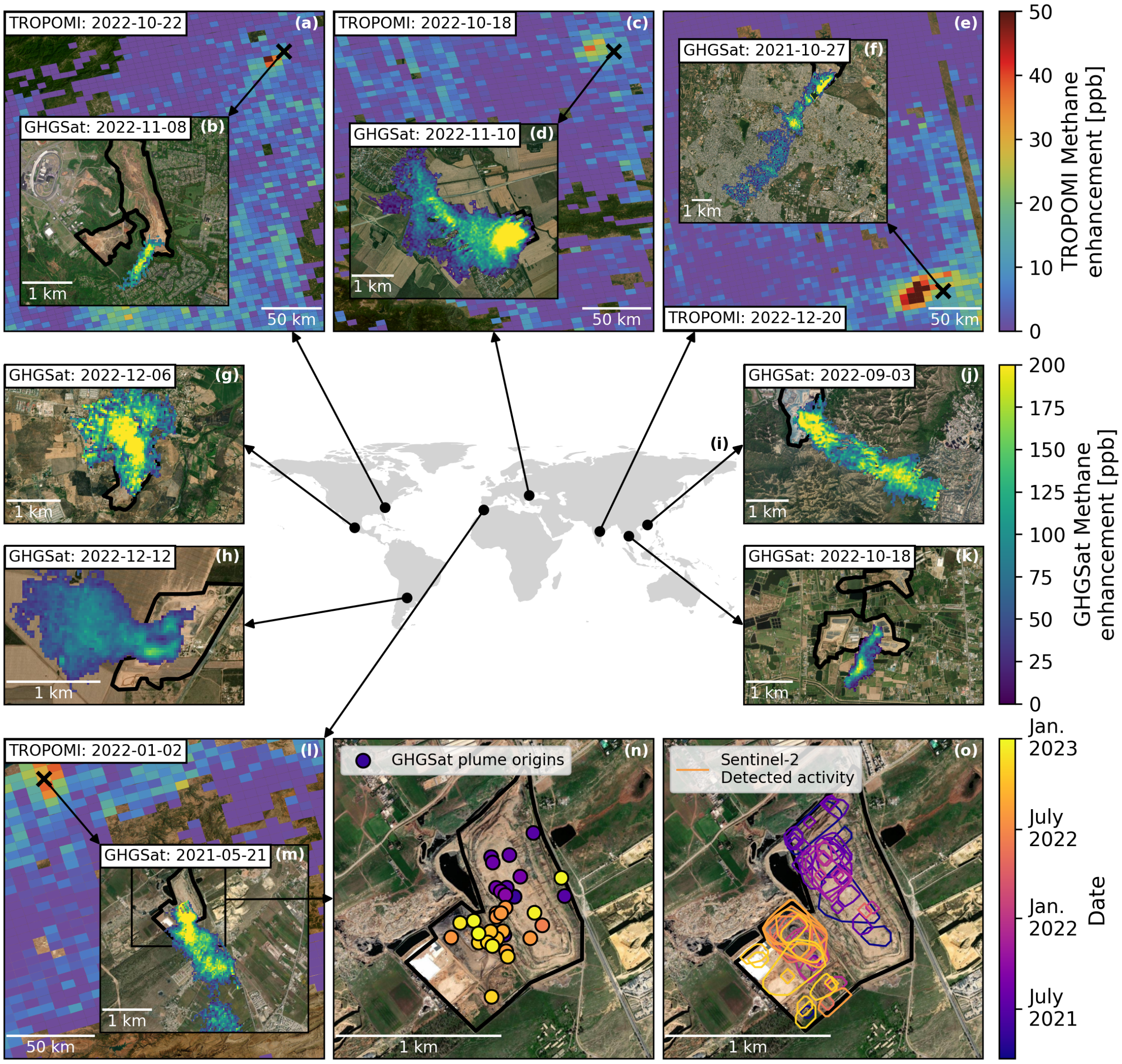

Figure 2. Examples of GHGSat facility-scale (panels b, d, f, g, h, j, k and m) and TROPOMI-detected urban area (panels a, c, e and l) methane emission plumes for Charlotte (USA, a, b), Bucharest (Romania, c, d), Hyderabad (India, e, f), Guadalajara (Mexico, g), Córdoba (Argentina, h), Hong Kong (China, j), Bangkok (Thailand, k) and Casablanca (Morocco, l, m) urban areas. The spatiotemporal distributions of all GHGSat plume origins and Sentinel-2 detected surface activity for the Casablanca landfill are shown in panels n and o, respectively. Black crosses show site locations and thick black contours highlight landfill site boundaries. Background images are retrieved from Esri World Imagery[39].

The median site-wise averaged emission rate is 1.3 t/hr (including null detections), with 5th and 95th percentiles of 0.1 t/hr and 6.9 t/hr, respectively (see Methods and Supplements). The lowest three site-averaged detected emission rates are found at a Canadian landfill in British Columbia (0.03±0.03 t/hr), an Italian landfill near Rome (0.04±0.03 t/hr) and at a South-African landfill near Gqeberha (0.06±0.04 t/hr). The highest three site-averaged detected emission rates are found at the Norte III landfill in Buenos Aires, Argentina (22.1±1.9 t/hr), at a landfill near Hong Kong, China (10.0±2.7 t/hr) and at a landfill near Tehran, Iran (9.4±4.9 t/hr). Using satellite and aerial imagery from Google Earth, we manually classify the 151 waste disposal sites into two categories: 108 managed landfills (sites that show organized structures to bury waste, for example featuring covers) and 43 dumping sites (that show informal gathering of waste). Managed landfills and dumping sites do not show statistically significant different detected emission rate distributions (see Figure 1 and Supplement S6). Overall, the distribution of site-wise averaged detected emissions is heavy-tailed, with the 60 (40%) strongest-emitting sites (47 managed landfills and 13 dumping sites) accounting for 80% of total emissions (see Supplements S4). This estimated skewness is probably conservative as the 100 kg/hr detection threshold and selective targeting of GHGSat would limit the inclusion of low-emitting sites. Overall, the 151 waste disposal sites observed here represent a small fraction of the global total number of landfills (over 10,000 are included in the Climate TRACE (Tracking Real-Time Atmospheric Carbon Emissions) coalition datasets[40]), but have a total detected methane emission rate of 2.9 million tons per year, which amounts to 7.4% of 2022 global solid waste emissions in version 8 of the Emissions Database for Global Atmospheric Research (EDGAR) inventory[3].

Figure 3 compares facility-level GHGSat-detected methane emission rates against national site-level reporting programs[41–43] and modeled emissions from the non-profit Climate TRACE coalition[40]. National reporting data exclusively cover managed landfills in the United States, Canada, and some European Union countries, while Climate TRACE has more global coverage and includes dumping sites (see Supplements S7). Overall, we find no correlation between satellite-based and reported or modelled data ($r = 0.04$ for reported emissions, and $r = 0.18$ for Climate TRACE), with differences showing an insignificant bias and a large scatter, exceeding the averaged emission rates (see Supplements S8). Analyzing managed landfills and dumping sites separately does not change this conclusion. Although no overall bias is found, emissions from 14 (out of 37) landfills are at least twice as large compared to what is reported to national programs. As the US Greenhouse Gas Reporting Program includes reports based on two different methodologies, one based on gas capture efficiency and the other based on waste decay modelling, we can compare our results for the US to both (Figure 3 separates US sites depending on which reporting method was chosen by the facilities). Comparing both estimates for all US landfills to GHGSat-detected emissions (See Supplements S9), we observe that the approach based on gas capture efficiency tends to underestimate emissions (by a factor 2) while the one based on waste decay modelling tends to overestimate them (by a factor 1.5). These US results are consistent with a recent investigation of landfill emission models used for reporting[44] and with aerial-based observations[38]. Neither method shows a strong correlation with our results. These findings highlight the critical importance of coordinating bottom-up modelling efforts with independent observations of landfill emissions to improve the understanding of facility-scale waste emissions.

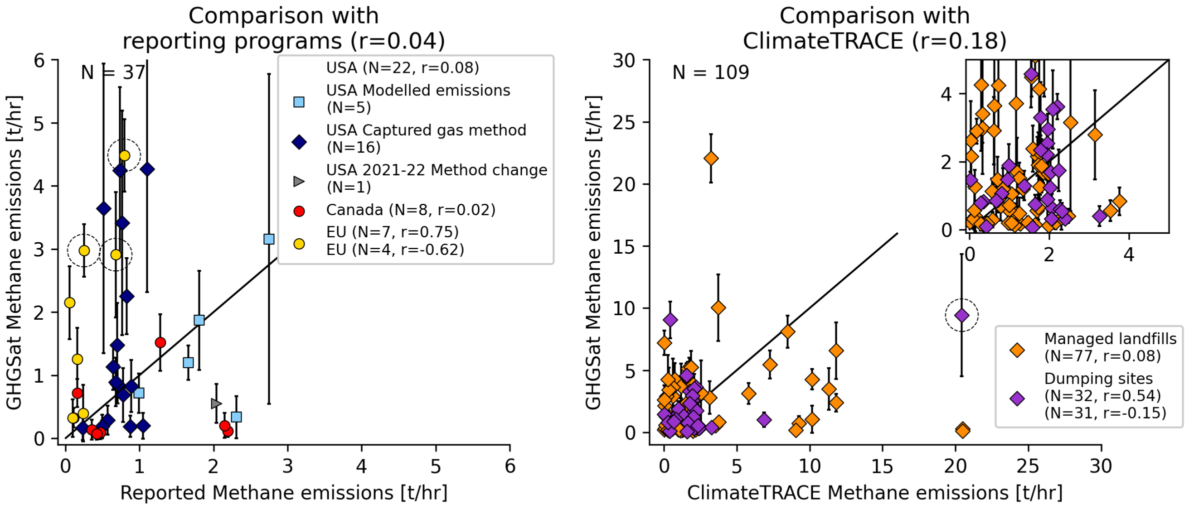

Figure 3. Comparison of site-wise methane emission rates observed by GHGSat against data included in reporting programs (left) and emissions calculated by the Climate TRACE non-profit (right), both averaged over the corresponding GHGSat observation years. Reported and Climate TRACE data are provided as annual totals and have been converted to hourly rates assuming constant emissions. Error bars show the site-wise averaged GHGSat emission uncertainty. The 1-to-1 line is shown in black. The circled sites in both panels drive the high correlations for EU site reports (r=0.75) and Climate TRACE dumping sites (r=0.54). If removed, these correlations drop to r=-0.62 and r=-0.15, respectively.

Our observations cover 47 different countries, with 46 (10 Annex-I and 36 non-Annex-I countries) that have reported national solid waste methane emissions to the United Nations Framework Convention on Climate Change (UNFCCC)[11]. To compare our site-level emissions with these national reports, we conservatively estimate the population serviced by each landfill[7,45] and calculate nationally averaged emission rates per capita (see Supplements S10 and S11). We find large country-to-country differences and limited correlation (r=0.24). While the estimation of people serviced by each landfill adds uncertainty, this result indicates further efforts must be undertaken to reconcile bottom-up and top-down understandings of national solid-waste methane emissions. As an illustration, for 9 countries (Bangladesh, Ecuador, Ethiopia, Honduras, India, Iran, Kenya, Thailand, Turkey), our GHGSat-based emission per capita estimates are more than twice as high as the ones from the UNFCCC, and total GHGSat-observed emissions exceed total UNFCCC emissions for Honduras and Iran. However, our results show an overall consistent picture when aggregated at global scale (weighted by each country's population): GHGSat-observed (3.1 – 6.4 kg/yr) and UN-reported emissions per capita (5.9 – 6.3 kg/yr) agree within their respective uncertainty estimates.

Figure 2 shows that high resolution observations also allow to pinpoint where detected emissions originate within a solid waste disposal facility. To understand these origins, we compare manually verified GHGSat emission plume origins with surface activity detected from clear-sky Sentinel-2 10-m resolution RGB observations (see Methods and Supplements S12, S13 and S14). A landfill near Casablanca (Morocco; Figure 2l-o), is a clear example, as both GHGSat plume sources and landfill surface activity show a North to South migration as time progresses and a new section of the landfill is developed in the southwest. Across 107 facilities that have enough clear-sky Sentinel-2 images and good quality surface activity detection results, we find that 44 (41%) show a statistically significant proximity (p-value<0.05) between surface landfill activity and GHGSat plume source location. When considering only the 21 sites for which at least 16 plume origins can be identified in GHGSat observations, we find statistically-significant proximity for 18 (86%) of them (See Supplements S14). This result is consistent with reports of methane emissions being observed originating from landfills' active areas and/or open modules in on-ground, airborne, and satellite-based studies[6,38,46,47]. This emphasizes the need to quantify emissions from the active surface, underscoring the importance of repeated observations to both reliably estimate mean emissions and to narrow down on (potentially migrating) source locations within a landfill. This spatial information can help focus mitigation efforts more effectively. Emissions from other sources near landfills can also be observed. While these sources were filtered from the analysis, examples include plumes from a wastewater treatment plant near Shanghai and a biogas plant linked to the Las Dehesas landfill in Madrid (Supplements S15).

Our survey has unprecedented spatial coverage that brings top-down observation-based estimates of methane emissions for 151 waste disposal sites across six continents. It sheds new light on the mitigation potential of urban methane emissions and on the ability of high-resolution satellites to monitor methane emissions from waste disposal sites and support mitigation activities by pinpointing emission sources within the facility, highlighting the importance of the active surface. We find that bottom-up and top-down satellite-based solid waste emission estimates cannot currently be reconciled at facility and country scales. This disagreement is consistent with previous facility-scale studies using aerial measurements[38] and country-scale studies using TROPOMI data[48,49]. These discrepancies highlight the importance of site-level data and practices, and call for additional efforts focused on both managed landfills and dumping sites, aiming to close this gap between current bottom-up and top-down understandings of methane emissions from solid waste. Ideally, such studies would involve partners operating waste disposal sites, bottom-up modelers, and ground, aerial and satellite-based methane observations. An improved understanding of site-level solid waste methane emissions can support more effective emission mitigation strategies contributing to the worldwide efforts against climate change.

Main text references

1. IPCC. Summary for Policymakers. Climate Change 2021: The Physical Science Basis. Contribution of Working Group I to the Sixth Assessment Report of the Intergovernmental Panel on Climate Change (2021) doi:10.1017/9781009157896.001.
2. Ocko, I. B. et al. Acting rapidly to deploy readily available methane mitigation measures by sector can immediately slow global warming. Environ. Res. Lett. **16**, 054042 (2021).
3. European Commission. EDGAR (Emissions Database for Global Atmospheric Research) Community GHG Database version 8.0. (2018).
4. Jacob, D. J. et al. Quantifying methane emissions from the global scale down to point sources using satellite observations of atmospheric methane. Atmospheric Chem. Phys. **22**, 9617–9646 (2022).
5. Schuit, B. J. et al. Automated detection and monitoring of methane super-emitters using satellite data. Atmospheric Chem. Phys. **23**, 9071–9098 (2023).
6. Maasakkers, J. D. et al. Using satellites to uncover large methane emissions from landfills. Sci. Adv. **8**, eabn9683 (2022).
7. Kaza, S., Yao, L. C., Bhada-Tata, P. & Woerden, F. V. What a Waste 2.0. (The World Bank Group, 2018).
8. IPCC. Summary for Policymakers. Global Warming of 1.5°C. An IPCC Special Report on the impacts of global warming of 1.5^\circC above pre-industrial levels and related global greenhouse gas emission pathways, in the context of strengthening the global response to the threat of climate change, sustainable development, and efforts to eradicate poverty 1–32 (2018).

9. Höglund-Isaksson, L., Gómez-Sanabria, A., Klimont, Z., Rafaj, P. & Schöpp, W. Technical potentials and costs for reducing global anthropogenic methane emissions in the 2050 timeframe –results from the GAINS model. Environ. Res. Commun. **2**, 025004 (2020).

10. Höglund-Isaksson, L. et al. Non-CO2 Greenhouse Gas Emissions in the EU-28 from 2005 to 2070: GAINS Model Methodology. https://pure.iiasa.ac.at/id/eprint/16977/ (2018).

11. United Nations Framework Convention on Climate Change. GHG data from UNFCCC. (2023).

12. Scharff, H. & Jacobs, J. Applying guidance for methane emission estimation for landfills. Waste Manag. **26**, 417–429 (2006).

13. Amini, H. R., Reinhart, D. R. & Mackie, K. R. Determination of first-order landfill gas modeling parameters and uncertainties. Waste Manag. **32**, 305–316 (2012).

14. Wang, Y. et al. Methane emissions from landfills differentially underestimated worldwide. Nat. Sustain. 1–12 (2024).

15. Nanda, S. & Berruti, F. Municipal solid waste management and landfilling technologies: a review. Environ. Chem. Lett. **19**, 1433–1456 (2021).

16. Mønster, J., Kjeldsen, P. & Scheutz, C. Methodologies for measuring fugitive methane emissions from landfills – A review. Waste Manag. **87**, 835–859 (2019).

17. Nisbet, E. G. et al. Methane Mitigation: Methods to Reduce Emissions, on the Path to the Paris Agreement. Rev. Geophys. **58**, e2019RG000675 (2020).

18. Varon, D. J. et al. Quantifying methane point sources from fine-scale satellite observations of atmospheric methane plumes. Atmospheric Meas. Tech. **11**, 5673–5686 (2018).

19. Varon, D. J. et al. High-frequency monitoring of anomalous methane point sources with multispectral Sentinel-2 satellite observations. Atmospheric Meas. Tech. **14**, 2771–2785 (2021).

20. Irakulis-Loitxate, I., Guanter, L., Maasakkers, J. D., Zavala-Araiza, D. & Aben, I. Satellites Detect Abatable Super-Emissions in One of the World's Largest Methane Hotspot Regions. Environ. Sci. Technol. **56**, 2143–2152 (2022).

21. Guanter, L. et al. Mapping methane point emissions with the PRISMA spaceborne imaging spectrometer. Remote Sens. Environ. **265**, 112671 (2021).

22. Roger, J. et al. High-Resolution Methane Mapping With the EnMAP Satellite Imaging Spectroscopy Mission. IEEE Trans. Geosci. Remote Sens. **62**, 1–12 (2024).

23. Thorpe, A. K. et al. Attribution of individual methane and carbon dioxide emission sources using EMIT observations from space. Sci. Adv. **9**, eadh2391 (2023).

24. Veefkind, J. P. et al. TROPOMI on the ESA Sentinel-5 Precursor: A GMES mission for global observations of the atmospheric composition for climate, air quality and ozone layer applications. Remote Sens. Environ. **120**, 70–83 (2012).

25. Lorente, A., Borsdorff, T., Martinez-Velarte, M. C. & Landgraf, J. Accounting for surface reflectance spectral features in TROPOMI methane retrievals. Atmospheric Meas. Tech. **16**, 1597–1608 (2023).

26. Pandey, S. et al. Satellite observations reveal extreme methane leakage from a natural gas well blowout. Proc. Natl. Acad. Sci. **116**, 26376–26381 (2019).

27. Lauvaux, T. et al. Global assessment of oil and gas methane ultra-emitters. Science **375**, 557–561 (2022).

28. Sadavarte, P. et al. Methane Emissions from Superemitting Coal Mines in Australia Quantified Using TROPOMI Satellite Observations. Environ. Sci. Technol. **55**, 16573–16580 (2021).

29. Tu, Q. et al. Quantifying CH_4 emissions in hard coal mines from TROPOMI and IASI observations using the wind-assigned anomaly method. Atmospheric Chem. Phys. **22**, 9747–9765 (2022).

30. Tu, Q. et al. Quantification of CH_4 emissions from waste disposal sites near the city of Madrid using ground- and space-based observations of COCCON, IASI. Atmospheric Chem. Phys. **22**, 295–317 (2022).

31. Varon, D. J. et al. Satellite Discovery of Anomalously Large Methane Point Sources From Oil/Gas Production. Geophys. Res. Lett. **46**, 13507–13516 (2019).

32. MacLean, J.-P. W. et al. Offshore methane detection and quantification from space using sun glint measurements with the GHGSat constellation. Atmospheric Meas. Tech. **17**, 863–874 (2024).

33. Varon, D. J., Jacob, D. J., Jervis, D. & McKeever, J. Quantifying Time-Averaged Methane Emissions from Individual Coal Mine Vents with GHGSat-D Satellite Observations. Environ. Sci. Technol. **54**, 10246–10253 (2020).

34. Hopkins, F. M. et al. Mitigation of methane emissions in cities: How new measurements and partnerships can contribute to emissions reduction strategies. Earths Future **4**, 408–425 (2016).

35. Young, A. Volumetric changes in landfill gas flux in response to variations in atmospheric pressure. Waste Manag. Res. **8**, 379–385 (1990).

36. Xu, L., Lin, X., Amen, J., Welding, K. & McDermitt, D. Impact of changes in barometric pressure on landfill methane emission. Glob. Biogeochem. Cycles **28**, 679–695 (2014).

37. Kissas, K., Ibrom, A., Kjeldsen, P. & Scheutz, C. Annual upscaling of methane emission field measurements from two Danish landfills, using empirical emission models. Waste Manag. **150**, 191–201 (2022).

38. Cusworth, D. H. et al. Quantifying methane emissions from United States landfills. Science **383**, 1499–1504 (2024).

39. Esri, Maxar, Earthstar Geographics & Community, the G. U. ESRI World Imagery. (2022).

40. Climate TRACE. Climate TRACE Emissions Inventory Tracking Real-time Atmospheric Carbon Emissions. (2023).

41. U.S. Environmental Protection Agency Office of Atmospheric Protection. Greenhouse Gas Reporting Program (GHGRP). (2023).

42. Government of Canada. Greenhouse Gas Reporting Program (GHGRP) - Facility Greenhouse Gas (GHG) Data. (2023).

43. European Environment Agency. European Pollutant Release and Transfer Register (E-PRTR). (2024).

44. Stark, B. M., Tian, K. & Krause, M. J. Investigation of U.S. landfill GHG reporting program methane emission models. Waste Manag. **186**, 86–93 (2024).

45. Columbia University, Center for International Earth Science Information Network, CIESIN. Gridded Population of the World, Version 4 (GPWv4): Population Density Adjusted to Match 2015 Revision UN WPP Country Totals, Revision 11. (2018) doi:10.7927/H4F47M65.

46. Cusworth, D. H. et al. Using remote sensing to detect, validate, and quantify methane emissions from California solid waste operations. Environ. Res. Lett. **15**, 054012 (2020).

47. Kumar, P. et al. Detection and long-term quantification of methane emissions from an active landfill. Atmospheric Meas. Tech. **17**, 1229–1250 (2024).

48. Chen, Z. et al. Methane emissions from China: a high-resolution inversion of TROPOMI satellite observations. Atmospheric Chem. Phys. **22**, 10809–10826 (2022).

49. Nesser, H. et al. High-resolution US methane emissions inferred from an inversion of 2019 TROPOMI satellite data: contributions from individual states, urban areas, and landfills. Atmospheric Chem. Phys. **24**, 5069–5091 (2024).

Methods

Automatic methane plume detection in TROPOMI data

The TROPOspheric Monitoring Instrument (TROPOMI)[24] on board the European satellite Sentinel-5 Precursor was launched in 2017. It observes backscattered sunlight in the near and shortwave infrared around the 0.76 µm O_2 and 2.3 µm methane bands. Total columns of methane are retrieved from these observations using a full-physics approach that accounts for the interfering impact of surface reflectance, aerosol, and other geophysical variables on the shortwave infrared signal (version 2.6.0)[25]. TROPOMI is a methane flux mapper that offers daily global coverage with a 7 x 5.5 km^2 spatial resolution at nadir. In addition to being used in long-term inverse analyses, its imaging capabilities enable to detect anthropogenic methane emission plumes that arise from the world's largest emitters[26]. We employ a two-step machine learning approach to explore TROPOMI data for methane emission plumes automatically[5]. We analyze and manually verify all plumes detected in 2021 and 2022 with estimated sources within 50 km from any of the landfills targeted by GHGSat. We apply the Integrated Mass Enhancement (IME) method[18] to quantify the methane emission rate and its uncertainty for each TROPOMI-detected plume as described in Schuit et al. (2023)[5].

Given TROPOMI's spatial resolution (7 x 5.5 km^2) compared to GHGSat's (25 x 25 m^2), we cluster the 151 landfills observed by GHGSat into 130 TROPOMI-relevant urban areas. For each urban area, we first apply a 2-sigma filter to remove outlier estimates that can be hampered by an unrepresentative plume mask due to variable meteorology or surface effects (e.g. plume masks truncated by clouds for lower estimates, etc.). Then, relying on the remaining TROPOMI plume detections, we report their mean detected urban-scale methane emissions and their standard deviation. These averages only cover emissions detected as strong plumes and are not representative of mean urban emissions but do provide an indication of urban mitigation potential. Not detecting a plume does not imply that there are no emissions: it means that concentrated emissions are lower than the ~8 t/hr TROPOMI plume detection threshold or that observation/geographical conditions did not allow a TROPOMI detection[5]. The discrepancy with mean emissions is verified for 4 different (above-average emitting and often detected) cities (Buenos Aires, Delhi, Mumbai and Lahore) where IME-based rates show a 7% - 47% overestimation (while agreeing within uncertainties) compared to urban-level methane emission estimates based on atmospheric inversions and TROPOMI data[6] (see Supplements S2).

GHGSat observations and emission quantification

GHGSat-C1 to -C5 instruments were launched between 2020 and 2022. These instruments estimate the methane column density at ~25 x 25 m^2 resolution over targeted 12 x 15 km^2 domains[50]. The GHGSat instruments have an empirically measured methane column precision range of 1.4 – 2.9 %[51], which allows them to observe emission plumes from point or very localized sources emitting more than ~100 kg/hr (this detection threshold increases with wind speed)[32]. Pixels exhibiting local spatially-correlated methane column enhancements above background are clustered together and considered to belong to a plume[31]. We apply the IME method[18] to estimate an emission rate Q based on a delineated plume and the local wind speed sampled from a meteorological model. We have:

$$Q = \frac{U_{eff}}{L} \sum_i \Delta X_{CH_{4},i} a_i$$

with U_{eff}, the effective wind speed, calibrated against the 10-m wind speed over a set of Large Eddy Simulations (LES); $L = \sqrt{\sum_i a_i}$, the plume length computed as the square-root of the plume total area; $\Delta X_{CH_{4,i}}$, the local enhancement above background of the methane total column for the i-th pixel included in the plume with area a_i. Here, we use an effective wind speed calibration specific to landfills, based on LES of area sources: $U_{eff} = 0.34 \times U_{10\,m} + 0.66$[6], where $U_{10\,m}$ is the 10-m wind speed sampled from the GEOS-FP meteorological reanalysis[52]. The emission rate uncertainty calculation includes contributions from (1) wind speed error; (2) methane column retrieval error; and (3) IME calibration error[31].

Estimating site-level GHGSat averages

For any individual waste disposal site observation during a single overpass by GHGSat, three outcomes are possible: (1) no plume is detected; (2) only one plume is detected; and (3) several plumes (arising from the same site) are detected. In the first case, we conservatively consider the emission rate to be equal to zero, with no uncertainty. In the second and third cases, we apply the IME method to each plume separately to quantify its emission rate and uncertainty. In the third case, we sum together all the detected plume emission rates (and sum their respective uncertainties quadratically) to obtain an emission rate for the whole site.

Given a set of observations for a waste disposal site, we employ a two-step random sampling approach to evaluate the site-level averaged emission rate and its uncertainty. First, in a bootstrapping approach, we randomly (N=1000) resample our set of observations by randomly picking single observations with replacement. This enables us to generate an ensemble of averaged emission rates for which we also compute corresponding uncertainties assuming that single observations are independent Gaussian variables. We then sample a

Gaussian distribution (N=1000) for all these ensemble elements relying on their respective rates and uncertainties. Finally, we report the mean and standard deviation across this two-step random sampling approach as averaged emission rate and its uncertainty. This method accounts for the single-observation uncertainties and is especially useful to handle bi- or multi-modal site-wise emission rate distributions that can have a peak at zero (all the observations without any detection) and one or several peaks for positive emission rate values (all the observations with detected plumes).

Comparison of GHGSat and reported or calculated emissions

For site-wise GHGSat-based methane emission rate comparison against site-wise reported values included within national reporting programs, we manually match sites based on addresses (no distance threshold is used). To compare site-wise GHGSat-based methane emission rates against values modeled by ClimateTRACE, we only select sites for which we find matches within a 2 km distance from GHGSat targets, and then only consider the facilities within these 2 km that show the minimum distance from GHGSat targets. Supplement S7 details the other data selection criteria specific to each dataset we compare to. Reported and Climate TRACE data are provided as annual totals and have been converted to hourly rates assuming constant emissions.

Comparison of GHGSat estimates and UNFCCC data

We collected UNFCCC solid waste emission reports for Annex-I countries from the UNFCCC flexible data query website[11]. For non-Annex-I countries, we explored UNFCCC flexible query results, the latest Biennial Update Reports and National Communications in order to find the most recent number (see Supplements S10). For non-Annex-I countries, in case several sources provide different values for the same most recent year, we conservatively choose the highest reported value. For each country, we use its UNFCCC report reference year to scale the emission amount by the total country population ratio between 2022 and its reference year, using the 2022-revision of the UN World Population Prospects (WPP) data[53].

For each country i, we use the population density predicted for 2020 from the 2015-revised UN WPP-Adjusted Population Density v4.11 dataset at 2.5-minute resolution[41] to compute its GHGSat-based emission rate per capita. Given all the landfills observed in a country i, we sum the population N_i living within a radius r from the closest GHGSat target within this country. We denote this quantity $N_i(r)$. We then compute the GHGSat-based emission per capita $E_i(r) = (\sum_j \bar{Q}_{i,j})/N_i(r)$, with $\bar{Q}_{i,j}$, the averaged emission rate for the j-th waste disposal site in country i. For UNFCCC emissions per capita, we divide total UNFCCC reported emissions by the total country population for the year 2020 as predicted in the 2015 revision of the UN WPP data[54].

To assess the relevant radius r from GHGSat targets over which to integrate density data, we rely on the 2018 World Bank 'What a Waste' report[7] which provides comprehensive data to better characterize waste production and management around the world. For 125 cities, they report the typical distance d between the city center and the main waste disposal site, with an average d_{ref} = 17.7 km. We conservatively use d_{ref} for our analysis, except for the countries that are represented in this dataset and that show a country-wise averaged distance that is larger than d_{ref}. The values provided by the World Bank only account for the distance between the city center and the main waste disposal site. To encompass the whole city population, assuming circular cities and waste disposal sites on city limits, we conservatively use $r = 2 \times d$ to integrate the population around GHGSat-observed targets (overlaps between targets are only counted once). To discuss the sensitivity of population scaling to r and derive an uncertainty estimate, we explore population-scaling for $r_{min} = 2 \times d - d_{ref}$ and $r_{max} = 2 \times d + d_{ref}$. The analysis is performed for r values rounded to increments of 10 km, so the maximum radius r considered for population scaling is at least 50 km (see Supplements S10).

Landfill surface activity detection from Sentinel-2 imagery

Managed landfills and dumping sites are active and constantly evolving as they accept new waste: they expand and their active surface(s) move(s) to accommodate the incoming waste. High-resolution visual imagery can be used to track the surface activities at waste disposal sites. To compare the spatio-temporal distributions of GHGSat-detected methane plumes origins and landfill activities, we devise an image analysis scheme to automatically detect surface activity from time series of clear-sky 10-m resolution Sentinel-2 satellite images of waste disposal sites.

For each of the 151 waste disposal sites observed by GHGSat, we convert the time series of Sentinel-2 clear sky visual RGB images to grayscale by using the National Television Standard Committee (NTSC) formula[55]:

$$Grayscale = 0.299 \times R + 0.587 \times G + 0.114 \times B$$

Then, we apply a 3-image moving filter (over time) based on local structural analysis[56,57] that determines surface activity in a given image as the overlap between structural changes that happened between this image and the previous one, and between this image and the next one. Using manually-outlined landfill masks based on the latest Google Earth imagery, we only consider surface activity that is detected within landfill boundaries, and use filters to ignore pixels associated with water, clouds, or cloud shadows. We smooth the raw activity map with a median filter to remove spatially inconsistent noise and only keep spatially consistent activity clusters. Individual activity clusters are then identified, outlined with convex hulls and stored as surface activity results. For each landfill, surface activity results are manually verified before being included in the analysis. Details and illustrations are provided in the Supplements S12, together with coverage statistics over all the 151 landfills targeted by GHGSat.

Comparison of landfill surface activity results and GHGSat methane plume origins

We manually pinpoint the approximate source of all GHGSat plumes, selecting multiple sources where appropriate. We use these source locations to compare to the Sentinel-2 based surface activity analysis.

For a given plume, we use as proximity metric the minimum distance between the manually-determined plume origin and the nearest outline of a surface activity cluster detected in the Sentinel-2 image that is closest in time. We set the metric to zero if a plume origin falls inside a detected activity cluster. Consequently, the lower the metric value, the closer the source is to a detected surface activity cluster. We also compute the same metric for N=10000 points randomly drawn within the landfill boundaries. This comparison is conservative because it is possible that GHGSat plumes show sources outside of landfill boundaries (their metric values have no upper boundary) whereas these random points can only be located inside (their metric values have an upper boundary).

For each site, we compute the averaged metric across all GHGSat-detected methane emission plumes and compare this result with the distribution of averaged metric values obtained for the N=10000 randomly drawn points. We then evaluate the p-value probability of randomly obtaining averaged metric values that are lower than the GHGSat-based result. We consider that GHGSat plume origins show a statistically significant proximity with detected landfill surface activity if we obtain a p-value lower than 0.05 (see Supplement S13).

The Supplements S14 showcase examples from different landfills and present an overview of p-value results for all landfills where surface activity could be detected.

Acknowledgements

We thank the Global Methane Hub for funding the 'Targeting Waste Emissions Observed from Space – Phase 1' project. MD acknowledges funding from the GALES project (grant no. 15597) of the Dutch Technology Foundation STW-NWO. MD and ALN acknowledge the NSO TROPOMI national program. SS acknowledges funding from the IMEO Studies program contract DTIE22-EN5036. We thank the team that realized the TROPOMI instrument and its data products, consisting of the partnership between Airbus Defence and Space Netherlands, KNMI, SRON, and TNO and commissioned by NSO and ESA. The Sentinel-5 Precursor and Sentinel-2 are part of the EU Copernicus program, and Copernicus (modified) Sentinel-5P data (2021-2022) and Sentinel-2 data (2020-2023) have been used.

Competing interests

The authors declare that they have no competing interests.

Author contributions

MD, JDM, and IA designed the study. MD performed the analysis and interpretation of TROPOMI and GHGSat methane plumes, as well as the Sentinel-2 activity detection analysis, under the supervision of JDM and IA. MG, DJ and JMK selected the GHGSat methane plumes and contributed to their analysis and interpretation. DJV performed and provided the effective wind speed calibration for landfills, and contributed to the result interpretation. BJS performed the plume detection in TROPOMI data and contributed to their analysis. SS and ALN contributed to the analysis of TROPOMI data. MD wrote this article with feedback from all co-authors.

Data availability

The Sentinel-5P TROPOMI data and Sentinel-2 data are available at the Copernicus Data Hub (https://dataspace.copernicus.eu). GEOS FP wind data can be downloaded from https://gmao.gsfc.nasa.gov/GMAO_products/. ERA5 and GEOS-CF meteorological data were sampled using Google Earth Engine. The GHGSat-detected methane plumes will be made available upon acceptance of this article, along with a TROPOMI plume detection table. Tables summarizing the results at site level for GHGSat, and at urban area level for TROPOMI are already included in the Supplements.

Additional method references

50. Jervis, D. et al. The GHGSat-D imaging spectrometer. Atmospheric Meas. Tech. **14**, 2127–2140 (2021).
51. Ramier, A. et al. High Resolution Methane Detection with the GHGSat Constellation. in GLOC 2023 conference proceedings (2023).
52. Molod, A. et al. The GEOS-5 Atmospheric General Circulation Model: Mean Climate and Development from MERRA to Fortuna. https://ntrs.nasa.gov/citations/20120011790 (2012).
53. United Nations, D. of E. & Social Affairs, P. D. World Population Prospects 2022 Revision. (2022).
54. United Nations, D. of E. & Social Affairs, P. D. World Population Prospects 2015 Revision. (2015).
55. Livingston, D. C. Colorimetric Analysis of the NTSC Color Television System. Proc. IRE **42**, 138–150 (1954).
56. Wang, Z., Bovik, A. C., Sheikh, H. R. & Simoncelli, E. P. Image quality assessment: from error visibility to structural similarity. IEEE Trans. Image Process. **13**, 600–612 (2004).
57. Wang, Z. & Bovik, A. C. Mean squared error: Love it or leave it? A new look at Signal Fidelity Measures. IEEE Signal Process. Mag. **26**, 98–117 (2009).

Supplements to

Satellite survey sheds new light on global solid waste methane emissions

Supplement S1: Discussion of plume-based IME estimates of emission rates against atmospheric inversion results

Figure S1.1 shows how averaged emission rates for four strongly-emitting cities relying on plume-based IME estimates, obtained from automated TROPOMI plume detections over 2021 and 2022 for this work, compare to posterior emission estimates obtained through atmospheric inversion performed for 2020 in Maasakkers et al., 2022[1]. The IME plume-based estimates show a positive bias as they only comprise data from days where emissions were high enough to allow for a plume detection, and lower emitting days that would have been accounted for in a comprehensive atmospheric inversion are not considered in this plume-based approach. This is why we consider that our plume-based IME estimates is more representative of the emission upper boundary rather than the actual average.

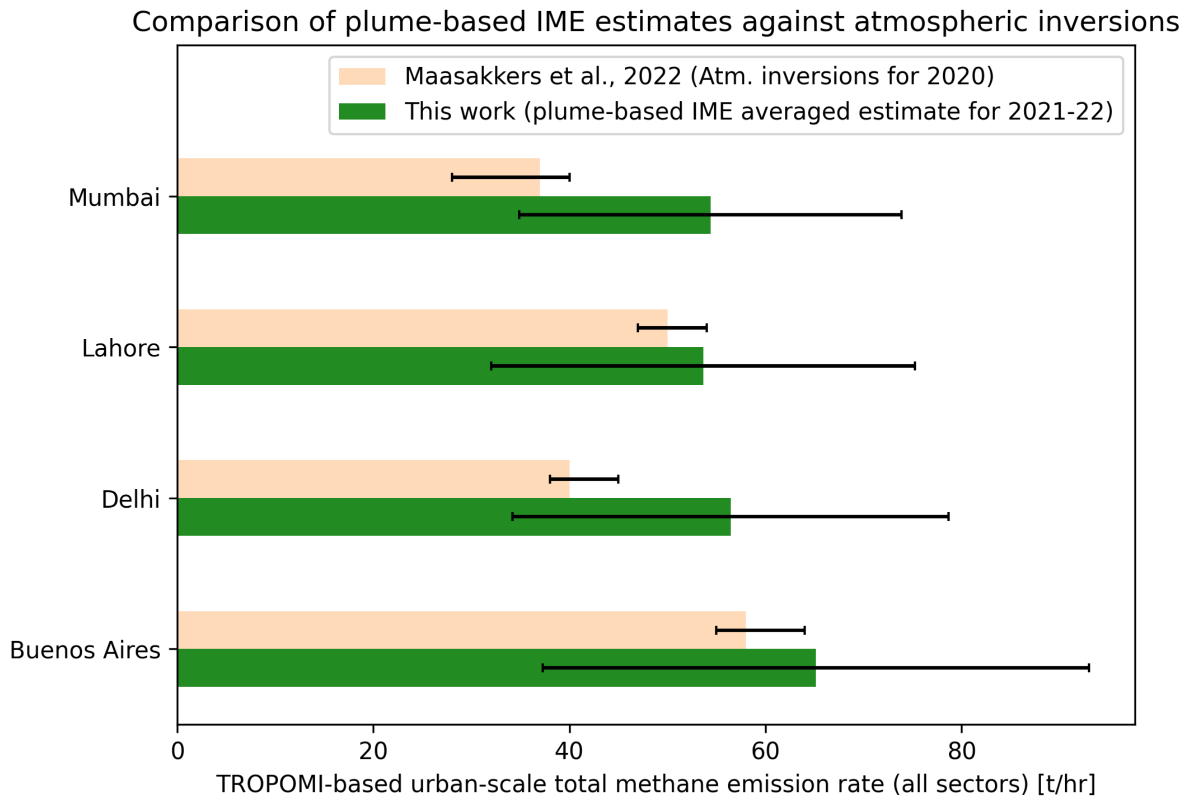

Figure S1.1. Comparison of plume-based IME estimates of total methane emission rates for four urban areas over 2021-2022 (this work) against atmospheric inversion results obtained for the same areas for 2020[1].

Supplement S2: Supplementary visuals, information and data on TROPOMI-based total urban-scale methane emissions

This supplement provides additional information on TROPOMI plume detections for the urban areas targeted by GHGSat. The median number of plume detections over two years is 6 (Figure S2.1) with only 14 cities accounting for more than 80% of all detections. These cities combine regular coverage with large emissions, leading to a high number of detected emission plumes. The cities are (sorted per country, themselves in alphabetical order):

- Argentina: Buenos Aires
- Bangladesh: Dhaka
- India: Delhi, Ahmedabad, Lucknow, Kanpur, Hyderabad, Mumbai, Kolkata
- Iran: Tehran
- Morocco: Casablanca
- Pakistan: Lahore, Karachi
- Spain: Madrid

Figure S2.2 provides the averaged plume-based IME emission rate estimates for all the 46 urban areas that show at least one plume detection over 2021-2022. These rates have a 19 t/hr median, with 5th and 95th percentiles of 5 t/hr and 74 t/hr, respectively. Table S2.1 provides TROPOMI plume-based emission rates for all urban areas that show at least one detected plume.

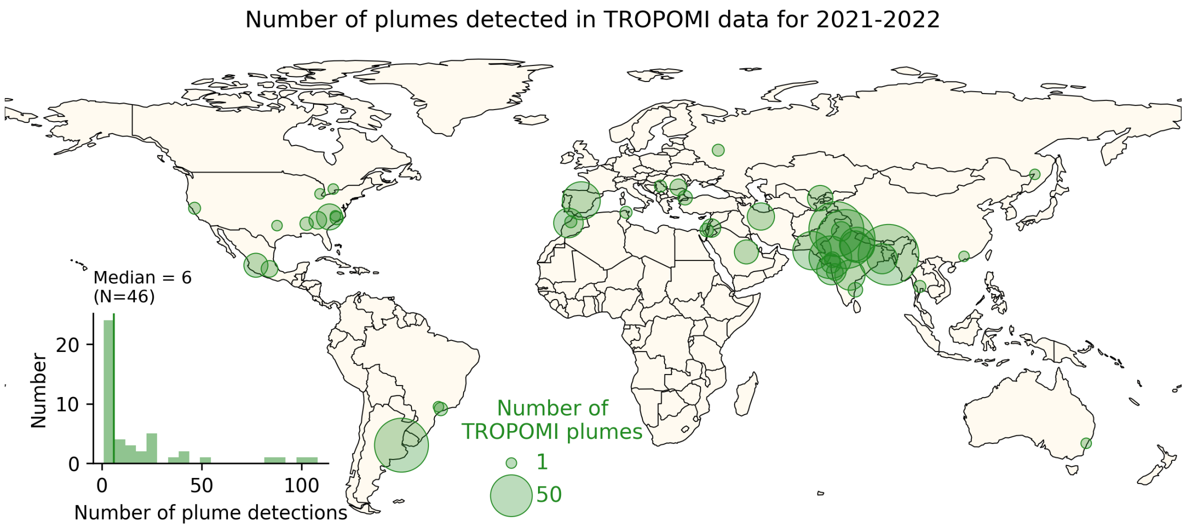

Figure S2.1 Spatial distribution of the methane plume detection number in TROPOMI data for urban areas targeted by GHGSat instruments.

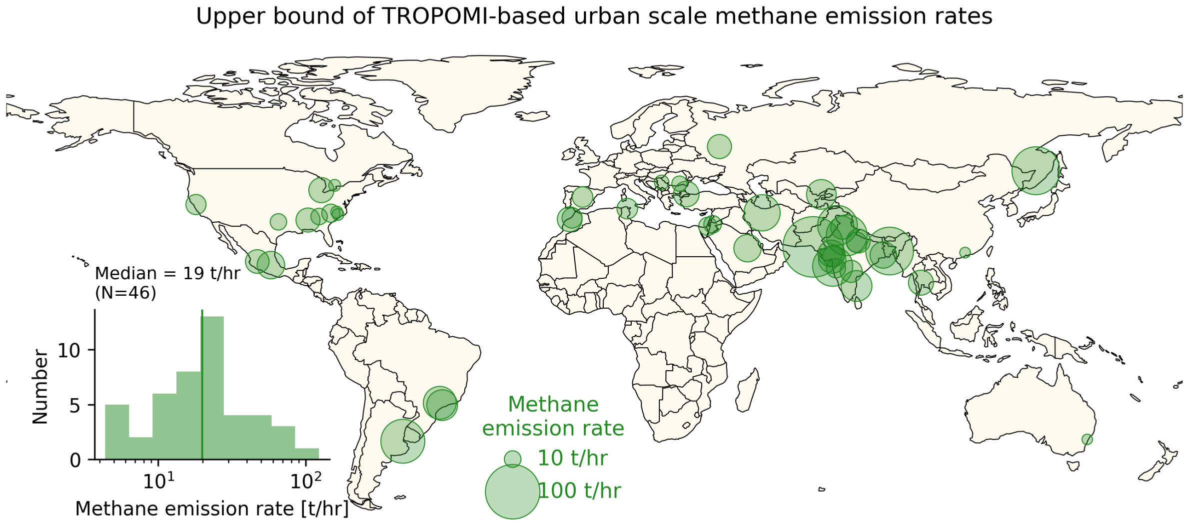

Figure S2.2 Spatial distribution of mean plume-based TROPOMI IME estimates of methane emission rate for the 46 urban areas targeted by GHGSat that show methane emission plumes in 2021-2022 TROPOMI data. As shown in Figure S1.1 for four cities, IME-based estimates relying on detected plumes provide an upper bound to actual average annual emissions.

Latitude	**Longitude**	**Country**	**City**	**N**	**N filtered**	**Q**	**Q_{uncert}**
° North	**° East**					**t/hr**	**t/hr**
20.5445	-103.1738	Mexico	Guadalajara	16	15	19.38	5.66
-34.5277	-58.6243	Argentina	Buenos Aires	87	85	65.15	27.86
-33.9544	150.8649	Australia	Sydney	1	1	4.38	1.55
23.7595	90.3763	Bangladesh	Dhaka	114	108	76.73	41.02
-23.4618	-46.5848	Brazil	São Paulo	3	3	32.34	10.54
-22.7509	-47.3149	Brazil	Campinas	1	1	36.88	20.83
43.8671	-79.5011	Canada	Toronto	1	1	5.38	3.94
23.2638	113.4822	China	Guangzhou	1	1	4.54	2.28
40.2925	-3.6102	Spain	Madrid	44	41	14.75	8.06
22.9826	72.5689	India	Ahmedabad	55	52	24.69	14.49
28.5694	77.2343	India	Delhi	108	102	56.43	22.23
21.1070	72.8056	India	Surat	9	9	25.75	4.97
22.2330	73.2068	India	Vadodara	5	5	16.16	5.11
22.5498	88.4343	India	Kolkata	26	25	24.19	12.68
19.0972	72.9412	India	Mumbai	26	24	54.39	19.50
18.4715	73.9509	India	Pune	6	6	13.09	3.28
30.9293	75.9071	India	Ludhiana	10	9	18.88	8.24
17.5181	78.5931	India	Hyderabad	27	25	17.00	6.76
13.0441	80.2461	India	Chennai	4	4	32.59	12.55
26.4490	80.2346	India	Kanpur	27	25	14.57	7.56
26.7970	80.7815	India	Lucknow	36	35	19.77	15.54
35.4587	51.3319	Iran	Tehran	21	20	44.69	10.35
31.3194	34.7371	Israel	Be'er Sheva	3	3	11.92	5.26
31.9312	36.1853	Jordan	Amman	9	8	11.06	3.90
33.4822	-7.5390	Morocco	Casablanca	25	24	21.29	6.51
33.8708	-6.8108	Morocco	Rabat	2	2	14.33	5.00
19.4399	-99.0060	Mexico	Mexico City	6	6	26.11	3.53
31.6273	74.4183	Pakistan	Lahore	93	88	53.64	21.60
25.0198	66.9782	Pakistan	Karachi	43	42	123.41	43.72
44.3968	26.0568	Romania	Bucharest	6	6	8.53	3.02

48.3639	135.1516	Russia	Khabarovsk	1	1	77.41	35.71
55.7535	38.2882	Russia	Moscow	2	2	20.15	4.11
24.6161	46.8914	Saudi Arabia	Riyadh	15	15	25.80	11.16
44.7848	20.5944	Serbia	Belgrade	2	2	7.75	2.05
14.0590	99.9718	Thailand	Bangkok	2	2	21.68	5.20
36.7379	10.0777	Tunisia	Tunis	2	2	14.88	1.72
41.2151	28.1497	Turkey	Istanbul	4	4	22.69	11.20
33.2430	-87.6518	United States	Tuscaloosa	3	3	20.05	1.93
37.9970	-121.9371	United States	Oakland	2	2	14.28	7.14
34.3274	-84.2442	United States	Atlanta	7	7	9.83	3.20
42.4023	-83.5555	United States	Detroit	1	1	21.76	9.87
35.3412	-80.6565	United States	Charlotte	18	18	11.78	5.92
34.9800	-78.4621	United States	Fayetteville	3	3	5.33	1.01
35.6757	-78.8478	United States	Raleigh	1	1	5.44	2.47
32.6824	-96.7085	United States	Dallas	1	1	9.73	7.99
41.0976	69.4832	Uzbekistan	Tashkent	18	17	30.29	17.73

Table S2.1. Summary of TROPOMI-based results for all urban areas that show at least one plume detection in 2021-2022 TROPOMI data. 'N' and 'N filtered' denote the number of detections obtained without and with filtering emission rates at 2σ. Q denotes the averaged TROPOMI plume-based emission rate, and Q_{uncert} the uncertainty.

Supplement S3: Explanations on TROPOMI urban hotspot coverage

The 151 landfills observed by GHGSat are located in 130 different urban areas, the relevant scale at which TROPOMI can resolve emissions. Out of those 130 urban areas, 46 show at least one manually-verified methane emission plume detection in TROPOMI data. Thus, most of targeted urban areas do not feature any detected TROPOMI methane plumes, which we explore in this Supplement.

For that purpose, we designed some metrics computed from the TROPOMI and GHGSat data, and the EDGAR emission inventory[2] to characterize each of these urban areas in terms of data coverage, surface roughness, albedo, and expected methane emissions. Table S3.1 describes these metrics. We determined empirical thresholds and boolean operations to label and list all the different reasons that can explain why TROPOMI data may not show any methane emission plume at a given location. Table S3.2 lists the boolean operations and thresholds used to label each urban area using our metrics. These thresholds do not perfectly separate urban areas with methane plumes from the ones with no detected plumes, but they draw a fair boundary between these two categories, also realizing the number of plume detections at a given location can vary due to different meteorological parameters (e.g. cloud cover, wind speed, etc).

Metric name	Definition
E_{GHGSat}	Total GHGSat-observed methane emission rate for the landfills included in the urban area, in t/hr
E_{EDGAR}	Total urban area methane emissions as reported in EDGAR v8 (all sectors) integrated over a 50 km radius from any GHGSat-observed landfill included in the urban area, in t/hr
C	Maximum number of TROPOMI overpasses with valid observations in 2 years (2021-2022) contained within a 0.3°x0.3° square centered on the considered landfill observed by GHGSat in the urban area, computed as a percentage of 730.5 observations (1 per day). This metric measures the overall coverage of TROPOMI over the urban area.
W_{small}	Fraction of 0.01°x0.01° oversampled pixels that show less than 75 valid observations over 2 years (2021-2022) within a 0.3°x0.3° image centered on the main landfill observed by GHGSat in the urban area. This metric assesses the area covered by waterbodies, sharp elevation changes and persistent cloudiness hampering TROPOMI coverage in the urban area.
W_{large}	Same as W_{small} but considering a 2°x2° image centered on the main landfill to assess coverage around the urban area.
R_{corr}	Pearson correlation coefficient between 0.3°x0.3° images oversampled at a resolution of 0.01°x0.01° of 2-year (2021-2022) averaged surface reflectance near 2.3 µm and 2-year average methane total column. This metric measures to what extent spatial albedo features may cause albedo-related artefacts in methane observations over the urban area.

Table S3.1. Metrics designed to characterize each urban hotspot in terms of expected methane emissions and TROPOMI data coverage and surface albedo.

Possible reason explaining why no TROPOMI plume is detected	**Boolean operation to verify**
Low mean coverage	$(C < 30)$
Missing data (due to water bodies, sharp elevation changes, persistent cloudiness, etc.)	$(W_{small} > 0.2)$ OR $(W_{large} > 0.4)$
Correlated albedo	$\lvert R_{corr} \rvert > 0.9$
Low emissions	$(E_{GHGSat} < 2$ t/hr) OR $(E_{EDGAR} < 8$ t/hr)

Table S3.2 Boolean operations that determine which possible reasons explain that no TROPOMI plume is detected for a given urban area.

For the 84 urban areas that do not show any plume in TROPOMI data, we only report the primary reason possibly explaining why, following the order of Table S3.2. Results are shown in Figure S3.1. We find that the absence of a detected plume can be explained by coverage-related issues for (26 + 36 =) 62 urban areas. These coverage issues can be persistent, due to waterbodies or sharp elevation changes near these urban areas, or depend on climate and meteorology with frequent cloudiness. Besides, for 3 urban areas, plume detections are hampered by sharp changes in surface albedo that cause methane total column retrieval errors correlated to albedo variations. These scenes are automatically rejected by our machine learning scheme as well[3]. Finally, given that TROPOMI has an overall 8 t/hr plume detection threshold[3], we find that low expected methane emissions explain the remaining urban areas where we do not detect any methane plume in TROPOMI data (N=19).

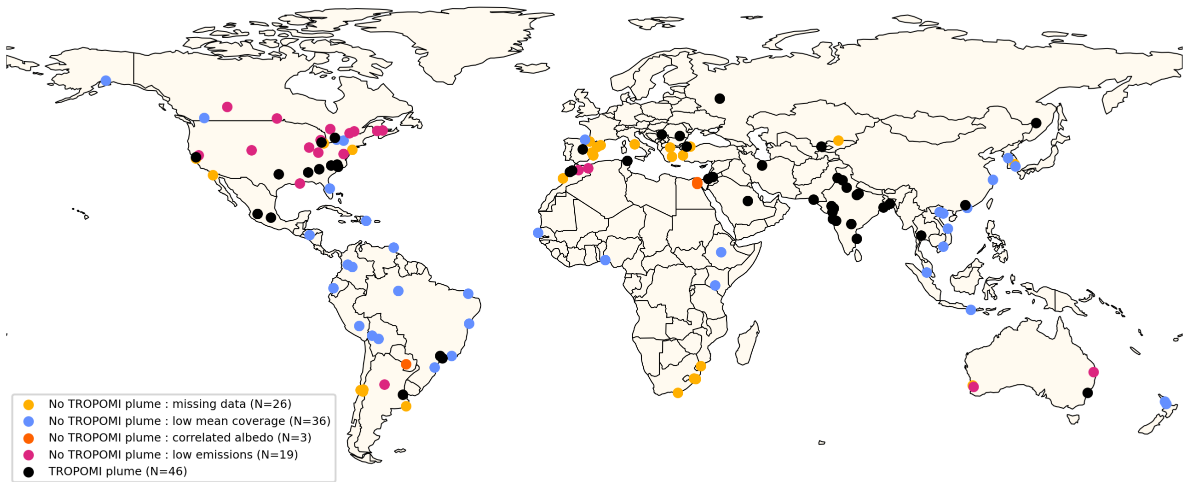

Figure S3.1 Spatial distribution of all 130 urban areas observed by GHGSat. Urban areas that show methane emission plumes detected in TROPOMI data are depicted in black. Colored urban areas do not show methane emission plumes detected in TROPOMI data, and their color depicts the prevailing explanation of why that is the case.

Supplement S4: Supplementary visuals and information on GHGSat-based facility-scale methane emissions

This supplement provides additional information on the set of GHGSat observations used in this work. Figure S4.1 shows the site-wise number of observations and Figure S4.2 the site-wise detection frequency. Figure S4.3 gives the distributions of the single-plume emission rates and their associated uncertainties, and draws the relationship between wind speed and single-plume emission rate uncertainty. Figure S4.4 gives the distributions of site-wise averaged emission rates and their associated uncertainties. Finally, Table S4.1 summarizes our results at site level.

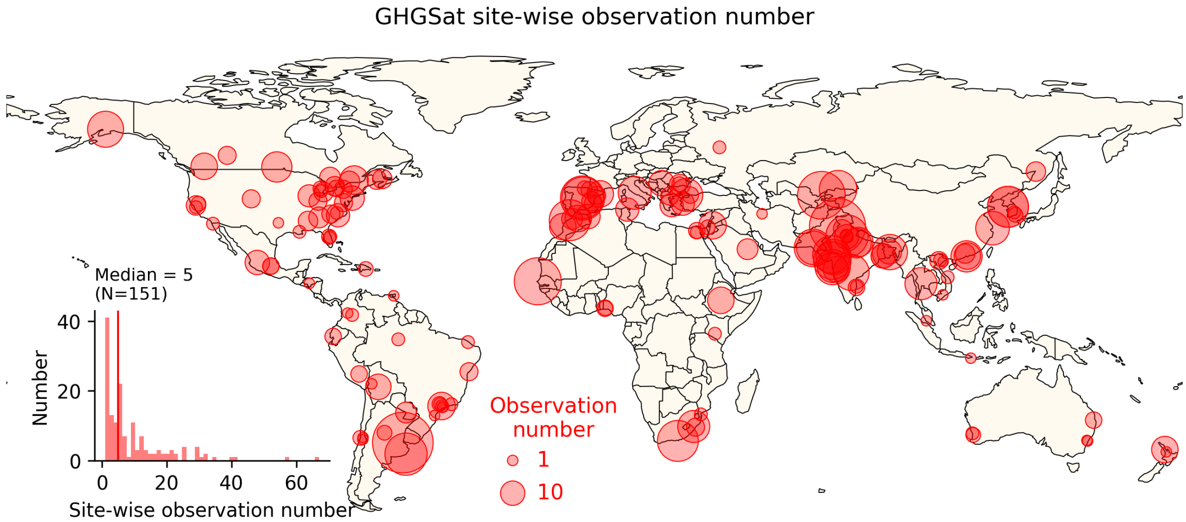

Figure S4.1 Spatial and site-wise observation count distributions of the 151 waste-disposal sites observed by GHGSat satellites. All sites have at least one plume detection.

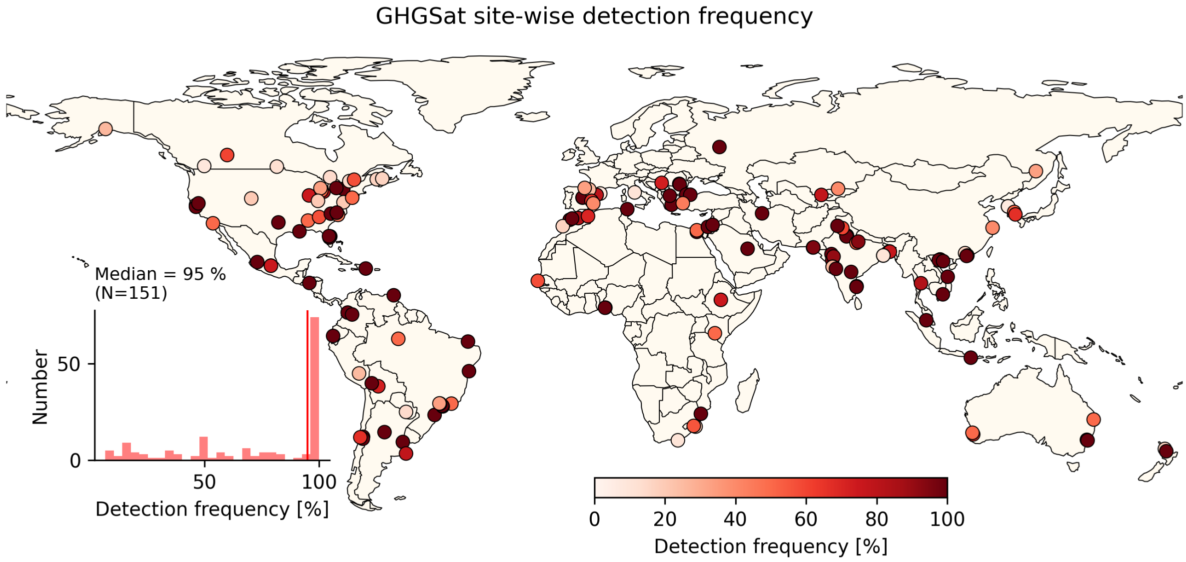

Figure S4.2. Spatial and site-wise detection frequency distributions of the 151 waste-disposal sites observed by GHGSat satellites. All sites have at least one plume detection.

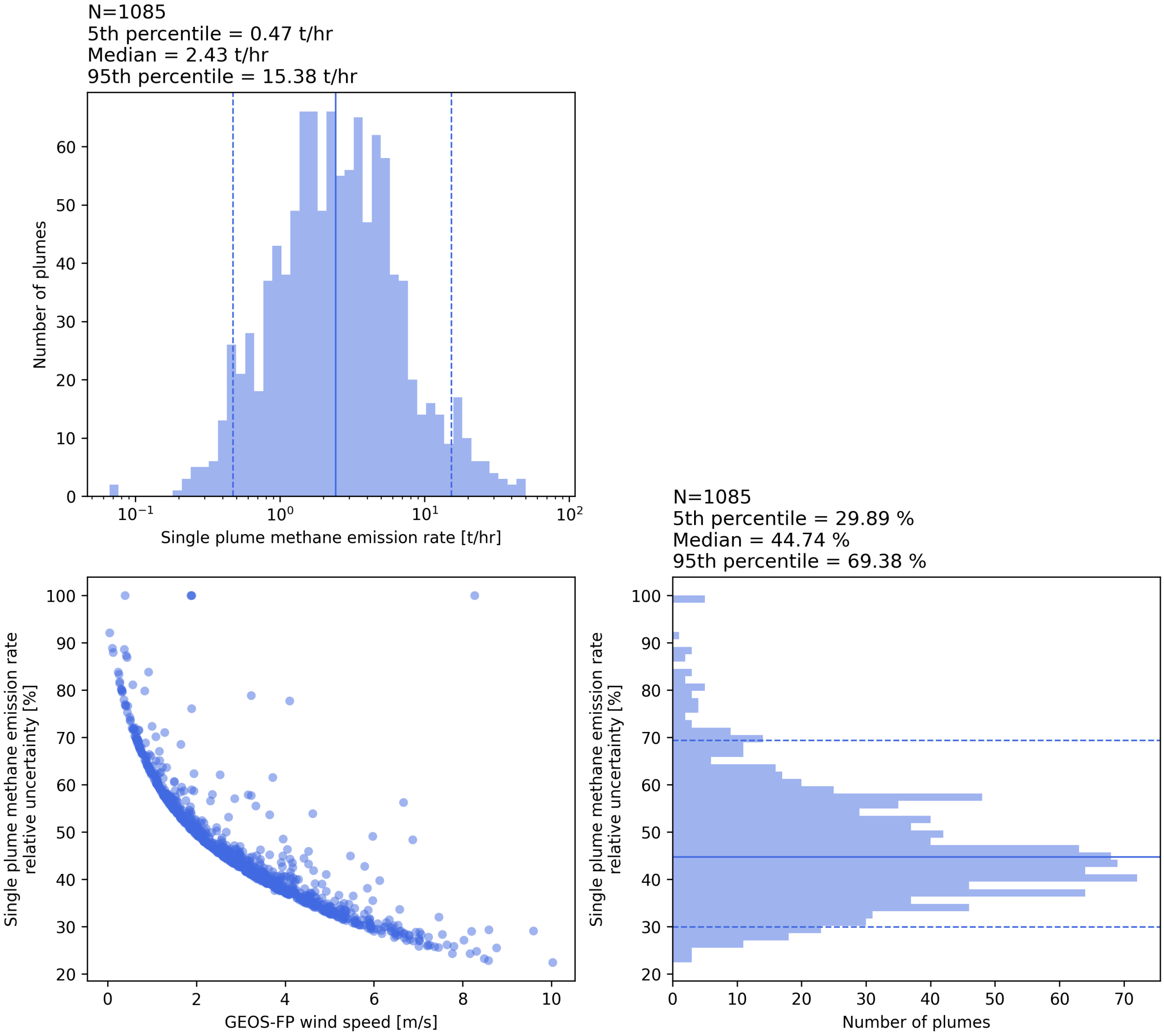

Figure S4.3. GHGSat Single plume methane emission rate (top left) and relative uncertainty (bottom right) distributions. The relationship between wind speed and the relative uncertainty for single plume emission rate is also given (bottom left).

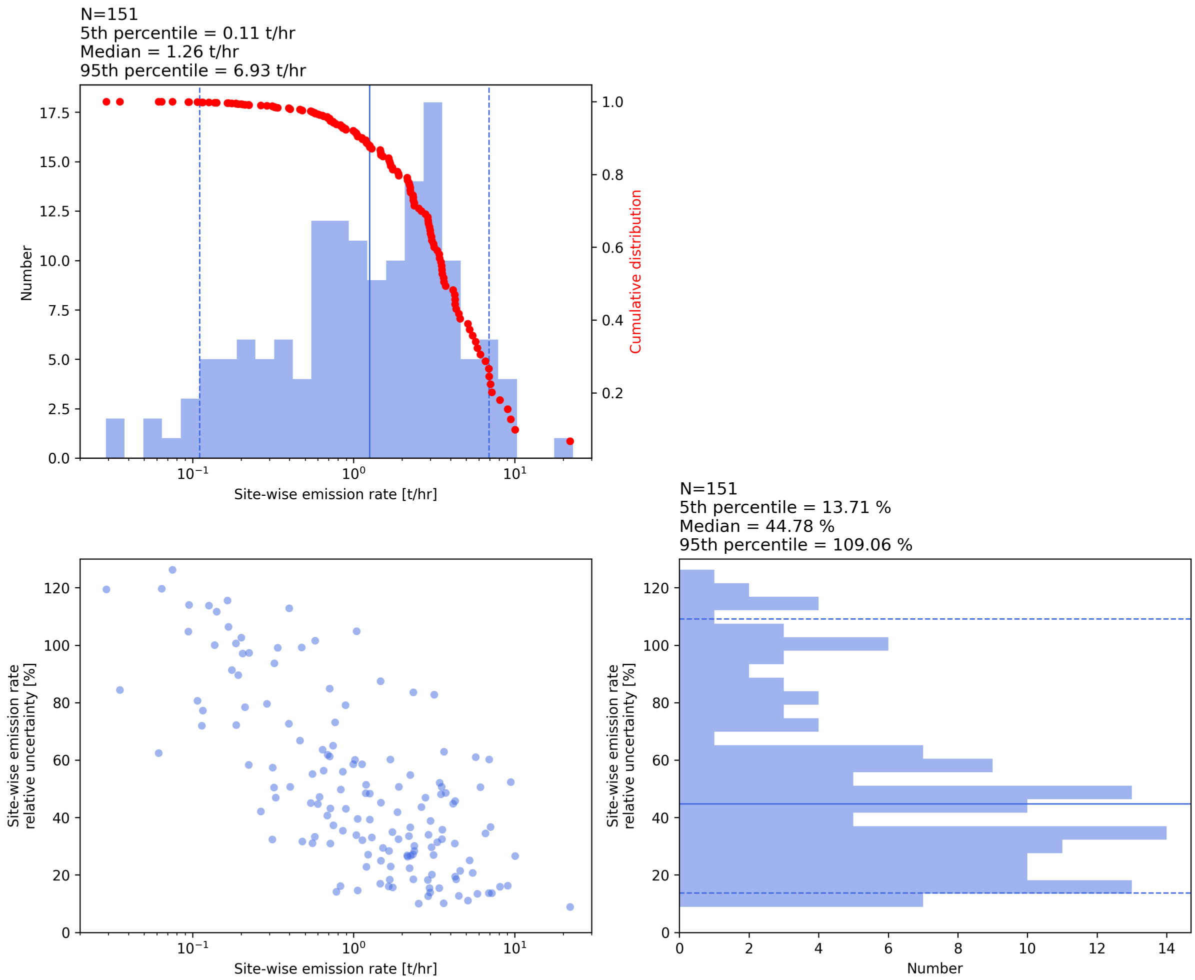

Figure S4.4. GHGSat site-wise averaged methane emission rate (top left) and relative uncertainty (bottom right) distributions. Relative uncertainties above 100% are related to sites showing one positive detection and a more numerous number of negative detections.

Site ID.	Lat	Lon	Country	N	Years	Q	Q_{unc}	Q_{RP}	Q_{CT}
	° N	° E				t/hr	t/hr	t/hr	t/hr
1	20.5445	-103.1738	Mexico	10	2022	2.38	0.72	-	11.82
2	32.4107	-116.7465	Mexico	2	2022	0.71	0.60	-	9.26
3	42.9284	-76.8487	United States	5	2022	4.25	1.32	0.74	0.73
4	-34.5277	-58.6243	Argentina	67	2021-22	22.07	1.95	-	3.23
5	-31.5172	-64.2325	Argentina	3	2022	2.16	0.57	-	1.70
6	-38.0676	-57.6486	Argentina	32	2021-22	1.06	0.15	-	1.05
7	-33.8639	150.7606	Australia	1	2022	1.69	1.02	-	1.19
8	-27.6621	152.8280	Australia	4	2022	0.46	0.31	-	1.15
9	-34.0449	150.9692	Australia	1	2022	3.72	1.81	-	1.17
10	-32.1958	115.9654	Australia	3	2022	0.22	0.13	-	0.01
11	-31.7057	115.7253	Australia	2	2022	0.17	0.16	-	1.27
12	23.7985	90.3013	Bangladesh	10	2021-22	4.58	0.98	-	1.54
13	23.7206	90.4513	Bangladesh	22	2021-22	2.22	0.50	-	-
14	-17.4766	-66.1273	Bolivia	11	2021-22	0.55	0.17	-	1.69

15	-16.5560	-68.1284	Bolivia	1	2022	1.26	0.61	-	1.76
16	-2.9551	-60.0121	Brazil	2	2022	1.47	1.28	-	-
17	-12.8558	-38.3734	Brazil	5	2022	1.67	0.31	-	1.85
18	-3.7953	-38.6823	Brazil	2	2022	3.13	0.85	-	5.80
19	-22.7930	-43.7556	Brazil	2	2022	2.35	1.96	-	-
20	-23.3450	-46.7718	Brazil	13	2021-22	4.33	0.80	-	-
21	-26.2496	-48.9024	Brazil	1	2022	0.71	0.44	-	-
22	-23.6368	-46.4220	Brazil	1	2022	4.14	1.86	-	1.75
23	-23.4037	-46.5605	Brazil	2	2022	3.54	1.26	-	-
24	-22.7784	-47.2058	Brazil	2	2022	5.73	3.50	-	-
25	-22.7234	-47.4239	Brazil	3	2022	0.14	0.14	-	1.65
26	53.3062	-112.3980	Canada	5	2021-22	0.33	0.15	0.11	-
27	49.9581	-119.4192	Canada	12	2022	0.03	0.03	-	-
28	49.7648	-97.1911	Canada	16	2021-22	0.12	0.09	2.19	1.98
29	45.8828	-66.6077	Canada	6	2022	0.14	0.16	0.36	0.34
30	46.0910	-64.9114	Canada	6	2021-22	0.09	0.11	0.47	-
31	42.0887	-82.8659	Canada	6	2021-22	1.52	0.45	1.28	1.25
32	43.8671	-79.5011	Canada	6	2021-22	0.20	0.20	2.15	2.16
33	46.5044	-80.9016	Canada	7	2022	0.06	0.08	-	-
34	45.3122	-74.9977	Canada	7	2021-22	0.08	0.09	0.42	-
35	45.7484	-73.5377	Canada	14	2021-22	0.72	0.22	0.16	-
36	-32.9521	-70.8010	Chile	1	2022	6.57	2.27	-	11.82
37	-33.5249	-70.8703	Chile	1	2022	2.79	1.31	-	3.14
38	-33.0898	-71.6372	Chile	3	2022	1.19	0.61	-	0.83
39	23.2638	113.4822	China	6	2021-22	1.04	1.09	-	10.17
40	22.5451	114.1701	China	12	2021-22	10.03	2.68	-	3.74
41	22.4176	113.9332	China	17	2021-22	8.10	1.29	-	8.47
42	31.0521	121.8871	China	20	2021-22	1.04	0.35	-	-
43	5.0812	-75.5047	Colombia	1	2022	0.65	0.37	-	1.73
44	4.4931	-74.1456	Colombia	2	2022	2.25	1.23	-	1.77
45	18.5618	-69.9699	Dominican Republic	3	2022	3.30	1.04	-	1.78
46	-2.0726	-79.9611	Ecuador	4	2022	3.00	1.17	-	-
47	29.7953	31.3558	Egypt	2	2022	2.33	0.63	-	-
48	30.2801	31.3582	Egypt	4	2022	0.40	0.29	-	3.26
49	41.5211	1.8066	Spain	12	2021-22	0.40	0.45	0.24	0.14
50	41.0783	0.6907	Spain	5	2022	0.69	0.28	-	-
51	40.2632	-3.6305	Spain	35	2021-22	4.48	0.57	0.79	1.55
52	40.3219	-3.5899	Spain	31	2021-22	2.98	0.42	0.25	0.33
53	42.7726	-1.5493	Spain	4	2022	0.32	0.30	0.10	0.10
54	43.2382	-2.9693	Spain	3	2022	0.57	0.58	-	0.12
55	39.2832	-0.8672	Spain	6	2022	1.26	0.49	0.16	0.14
56	38.4865	-0.3394	Spain	5	2022	0.75	0.48	-	-
57	8.9776	38.7121	Ethiopia	12	2021-22	1.47	0.37	-	0.95
58	38.0722	23.6496	Greece	9	2022	4.26	0.83	-	10.18
59	40.8490	23.0803	Greece	5	2022	2.91	0.99	0.68	0.61
60	14.1494	-87.2238	Honduras	1	2021	0.64	0.41	-	2.06
61	-8.7225	115.2222	Indonesia	1	2022	1.89	0.62	-	0.99
62	22.9826	72.5689	India	25	2021-22	3.62	0.37	-	2.20
63	28.7428	77.1552	India	2	2022	1.29	0.43	-	1.38
64	28.6227	77.3260	India	32	2021-22	2.54	0.26	-	1.95
65	28.5096	77.2841	India	2	2021	2.21	0.74	-	1.93

66	21.1070	72.8056	India	25	2021-22	2.89	0.37	-	0.17
67	22.2330	73.2068	India	22	2022	0.83	0.13	-	0.35
68	28.4026	77.1719	India	10	2021-22	1.46	0.25	-	0.02
69	22.5363	88.4241	India	10	2021-22	1.69	0.39	-	2.03
70	22.5633	88.4444	India	10	2021-22	0.09	0.10	-	0.41
71	19.1241	72.9526	India	22	2021-22	9.06	1.47	-	0.44
72	19.0703	72.9298	India	16	2021-22	0.32	0.16	-	2.40
73	18.4715	73.9509	India	11	2022	0.78	0.11	-	0.28
74	30.9293	75.9071	India	5	2022	0.61	0.29	-	-
75	17.5181	78.5931	India	23	2021-22	6.91	0.95	-	-
76	13.1352	80.2678	India	2	2022	1.74	0.61	-	2.24
77	12.9530	80.2245	India	4	2022	3.53	1.15	-	2.08
78	26.4490	80.2346	India	15	2022	0.60	0.27	-	2.27
79	26.7970	80.7815	India	15	2022	1.65	0.26	-	-
80	35.4587	51.3319	Iran	1	2022	9.43	4.93	-	20.44
81	31.3194	34.7371	Israel	3	2022	3.52	1.79	-	-
82	41.8542	12.3392	Italy	19	2021-22	0.04	0.03	-	-
83	31.9312	36.1853	Jordan	13	2022	5.46	1.13	-	7.26
84	-1.2486	36.8959	Kenya	2	2022	0.89	0.70	-	1.95
85	42.9676	74.5909	Kyrgyzstan	25	2021-22	0.31	0.10	-	2.05
86	37.5754	126.5988	South Korea	30	2021-22	0.27	0.11	-	20.50
87	37.5798	126.6210	South Korea	30	2021-22	0.11	0.09	-	20.50
88	35.8749	128.5181	South Korea	2	2022	0.48	0.47	-	1.25
89	35.1252	128.8742	South Korea	3	2022	1.13	0.66	-	-
90	34.0040	-4.9351	Morocco	12	2021-22	1.65	0.47	-	1.98
91	33.4822	-7.5390	Morocco	30	2021-22	5.11	0.57	-	1.64
92	31.5206	-9.6627	Morocco	12	2021-22	0.19	0.14	-	-
93	34.5802	-1.9442	Morocco	10	2021-22	0.57	0.19	-	0.99
94	33.8708	-6.8108	Morocco	7	2021-22	3.40	0.53	-	-
95	19.4582	-99.0170	Mexico	4	2021-22	1.90	0.97	-	1.72
96	19.4216	-98.9950	Mexico	4	2021-22	0.99	0.58	-	6.88
97	-25.8999	32.5973	Mozambique	2	2022	1.06	0.42	-	0.80
98	2.7327	101.6038	Malaysia	1	2022	6.94	4.18	-	-
99	6.5963	3.3746	Nigeria	3	2021-22	1.23	0.33	-	2.02
100	6.5630	3.2531	Nigeria	4	2022	0.75	0.28	-	1.64
101	-36.6592	174.6237	New Zealand	12	2021-22	0.21	0.17	-	1.46
102	-37.3693	175.0583	New Zealand	1	2021	0.40	0.20	-	2.47
103	31.6273	74.4183	Pakistan	57	2021-22	5.87	0.79	-	-
104	25.0099	66.9236	Pakistan	25	2022	0.48	0.15	-	-
105	25.0297	67.0328	Pakistan	20	2021-22	2.95	0.46	-	1.96
106	-13.5506	-72.0169	Peru	4	2022	0.13	0.14	-	1.13
107	-25.3289	-57.6425	Paraguay	7	2021-22	0.22	0.22	-	-
108	44.4785	25.9851	Romania	3	2022	0.77	0.56	-	-
109	44.3152	26.1285	Romania	7	2022	2.15	0.58	0.05	0.05
110	48.3639	135.1516	Russia	6	2022	0.11	0.08	-	-
111	55.7535	38.2882	Russia	2	2022	3.03	0.90	-	-
112	24.6161	46.8914	Saudi Arabia	7	2022	5.23	1.31	-	1.88
113	14.8024	-17.3131	Senegal	40	2021-22	2.34	0.43	-	1.78
114	44.7848	20.5944	Serbia	11	2021-22	2.38	0.68	-	1.59
115	14.0590	99.9718	Thailand	18	2021-22	2.89	0.53	-	-
116	10.3753	-61.4098	Trinidad and Tobago	1	2022	1.19	0.58	-	-

117	36.7379	10.0777	Tunisia	9	2022	3.05	0.61	-	-
118	41.2151	28.1497	Turkey	19	2022	7.21	0.99	-	0.03
119	41.1477	29.3709	Turkey	4	2022	3.48	1.68	-	11.31
120	38.5329	27.0682	Turkey	9	2022	0.86	0.48	-	0.66
121	61.2903	-149.6054	United States	23	2021-22	0.69	0.43	0.78	0.78
122	33.2430	-87.6518	United States	6	2021-22	0.31	0.18	-	2.06
123	37.9970	-121.9371	United States	6	2021	0.29	0.23	0.57	0.57
124	37.4581	-121.9416	United States	2	2021	1.48	0.67	0.70	0.70
125	38.5213	-121.1857	United States	3	2021	0.86	0.30	0.70	0.70
126	40.0177	-105.0143	United States	5	2021-22	0.19	0.19	0.50	0.44
127	28.4000	-80.8275	United States	2	2021-22	3.16	2.61	2.75	2.53
128	28.0581	-81.0973	United States	2	2021-22	3.64	2.29	0.52	0.62
129	28.4734	-81.2225	United States	3	2022	3.41	1.78	0.76	0.33
130	34.3274	-84.2442	United States	7	2021-22	0.55	0.31	2.04	3.53
131	40.9375	-87.3380	United States	8	2021-22	1.13	0.36	0.64	0.57
132	29.9343	-90.2610	United States	2	2021	4.26	1.95	1.10	0.29
133	38.8536	-76.7885	United States	5	2021-22	0.16	0.19	0.24	0.28
134	42.4023	-83.5555	United States	2	2022	0.19	0.17	0.87	0.98
135	43.1734	-83.8347	United States	3	2021	0.34	0.33	2.31	2.31
136	35.3412	-80.6565	United States	5	2022	2.25	0.60	0.83	-
137	34.9800	-78.4621	United States	9	2021-22	0.83	0.41	0.89	3.76
138	35.6757	-78.8478	United States	2	2022	0.89	0.38	0.68	0.72
139	40.2387	-74.1144	United States	10	2021-22	0.72	0.31	0.99	1.00
140	43.2100	-78.9745	United States	4	2022	1.20	0.27	1.66	1.34
141	39.2804	-84.5965	United States	5	2021	0.20	0.21	1.05	1.05
142	32.6824	-96.7085	United States	1	2021	1.87	0.78	1.81	1.81
143	41.0976	69.4832	Uzbekistan	41	2021-22	1.75	0.27	-	-
144	16.0423	108.1423	Vietnam	2	2022	2.63	1.15	-	0.03
145	10.6675	106.6724	Vietnam	1	2022	6.12	3.10	-	-
146	21.3361	105.8344	Vietnam	2	2022	7.08	2.60	-	-
147	21.1293	105.4232	Vietnam	5	2022	2.25	0.82	-	-
148	20.8150	106.7551	Vietnam	1	2022	1.02	0.61	-	-
149	-29.8179	30.9800	South Africa	5	2021-22	0.17	0.18	-	9.04
150	-34.0175	25.5669	South Africa	30	2021-22	0.06	0.04	-	1.57
151	-29.6066	30.4185	South Africa	18	2021-22	0.54	0.24	-	2.32

Table S4.1. Summary of site level GHGSat results. ‘Lat’ and ‘Lon’ denote ‘Latitude’ and ‘Longitude’; ‘N’ gives the number of GHGSat observations per site and ‘Years’ the years they cover. 'Q' and ‘Q_{unc}’ give the average emission rates and uncertainties, respectively. Q_{RP} provides reported emission rates in national reporting programs (if available) and Q_{CT} provides the emission rate computed by the ClimateTRACE initiative (if available).

Supplement S5: Analysis of possible meteorological drivers and seasonality of methane emissions from waste disposal sites

This supplement explores the possible drivers of methane emissions from waste disposal sites by meteorology and seasonality.

Figure S5.1 shows methane emission rate deviations from site-wise medians against meteorological parameter deviations from the median, for different meteorological parameters (panels (a) to (e)), and against seasons (panel (f)). All panels also include first-order sensitivity indices S_i that describe the amount of variance explained by each parameter[4]. Overall, we conclude from the very low first-order sensitivity indices S_i displayed in Figure S5.1 that none of the explored meteorological parameters shows convincing signs of driving emissions.

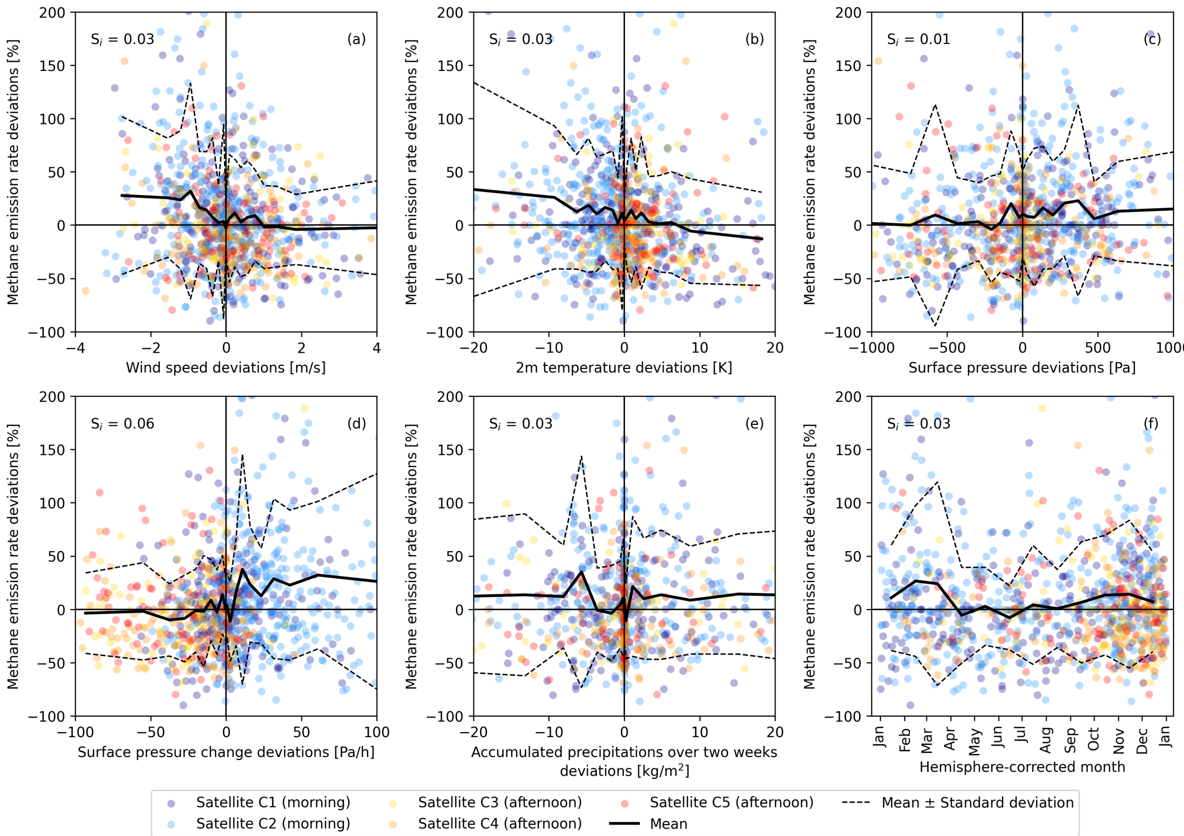

Figure S5.1. Methane emission rate deviations from site-wise medians (computed excluding null detections) against deviations from site-wise medians (computed excluding null detections) for wind speed (a), 2m air temperature (b), surface pressure (c), change in surface pressure (d), accumulated precipitations over two weeks (e) and month number in the year (corrected for hemisphere). All meteorological data are sampled from ERA5[5]. Smoothed mean curves are shown (thick black lines) and are used to compute first-order sensitivity indices S_i following[4]. Smoothed mean curves ± local standard deviation are also shown (thin dashed lines).

Supplement S6: Comparison of managed landfills and dumping site averaged site-wise emission rate distributions

This supplement provides a comparison of site-wise averaged emission rate distributions for managed landfills and dumping sites. First, Figure S6.1 compares raw averaged emission rates and no-detection frequency between managed landfill and dumping sites. Two-sided two-sample Kolmogorov-Smirnov tests are performed and yield non-significant p-values. This means that GHGSat-based methane emission rate distributions for managed landfills and dumping sites are not significantly different.

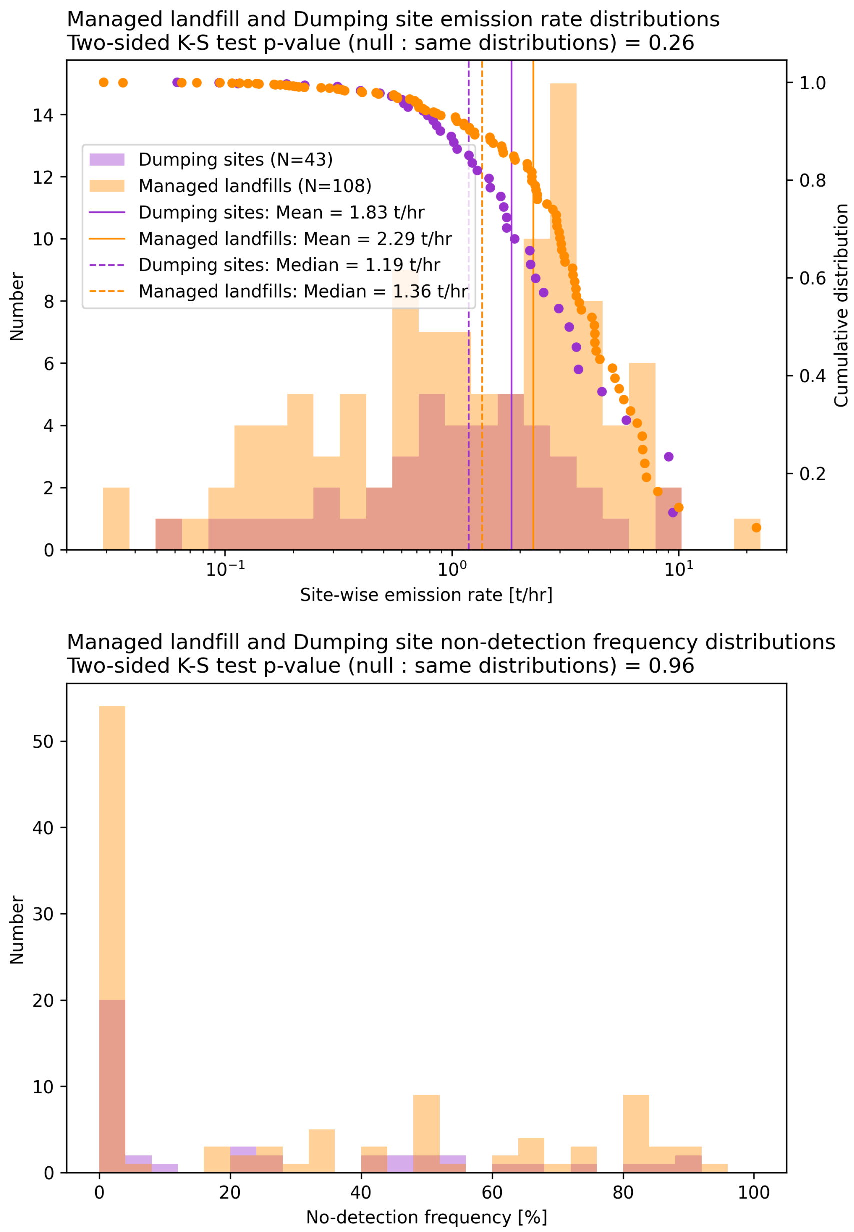

Figure S6.1 Comparison of site-wise emission (top) and no-detection frequency (bottom) distributions between managed landfills (orange) and dumping sites (purple).

We perform this comparison in two additional configurations to assess the impact of accounting for waste disposal site size when comparing managed landfill and dumping site emission rate distributions. Figure S6.2 showcases the same comparison as in Figure S6.1, but for emission rates per km^2, using both the total waste disposal site area (determined from Google Earth imagery as detailed in Supplement S12) and the total Sentinel-2 detected surface activity area (see details in Supplements S12, S13, S14, total site area has been used for sites without satisfying Sentinel-2 detected surface activity results) as area reference. Considering the low p-value (0.01) in the two-sided two-sample Kolmogorov-Smirnov evaluation for emission per area using total site area as reference, we conclude that emission per area distributions are not comparable between managed landfills and dumping sites, with dumping sites showing significantly higher emissions per area. This may be explained by the fact that managed landfills include closed inactive modules that show no emissions above GHGSat detection threshold but still add to the total site area whereas, by definition, dumping sites do not show these closed inactive modules. However, such a result does not hold when using the total Sentinel-2 detected surface activity area as the reference (p-value = 0.25). This result means that, in this dataset, managed landfills show non-significant emission rate distribution differences compared to dumping sites if only their active surfaces are considered. This points towards landfill management and emission mitigations measures being more efficient for closed modules that show no activity than for active ones that are in operation.

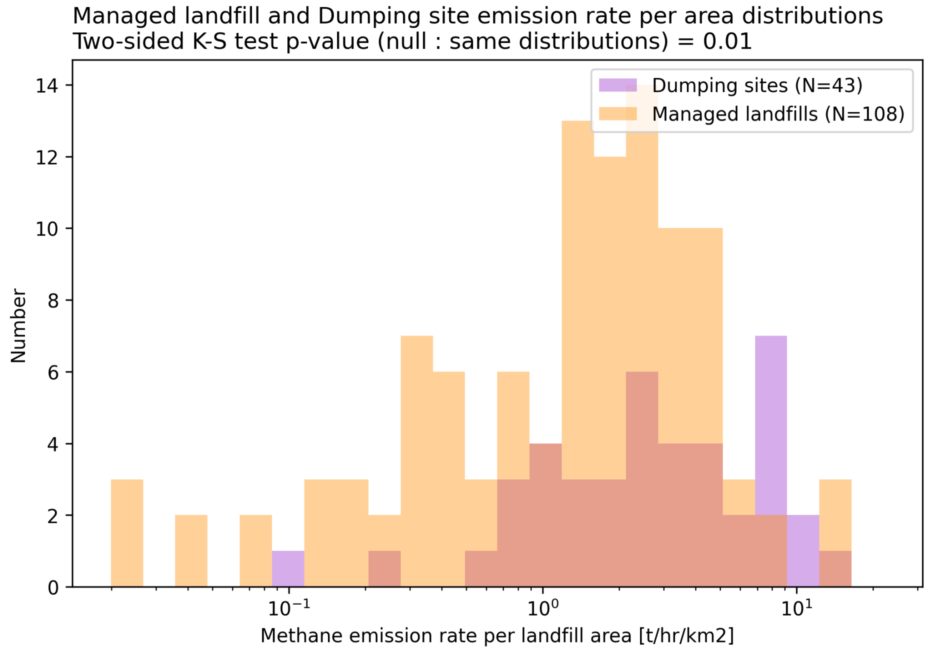

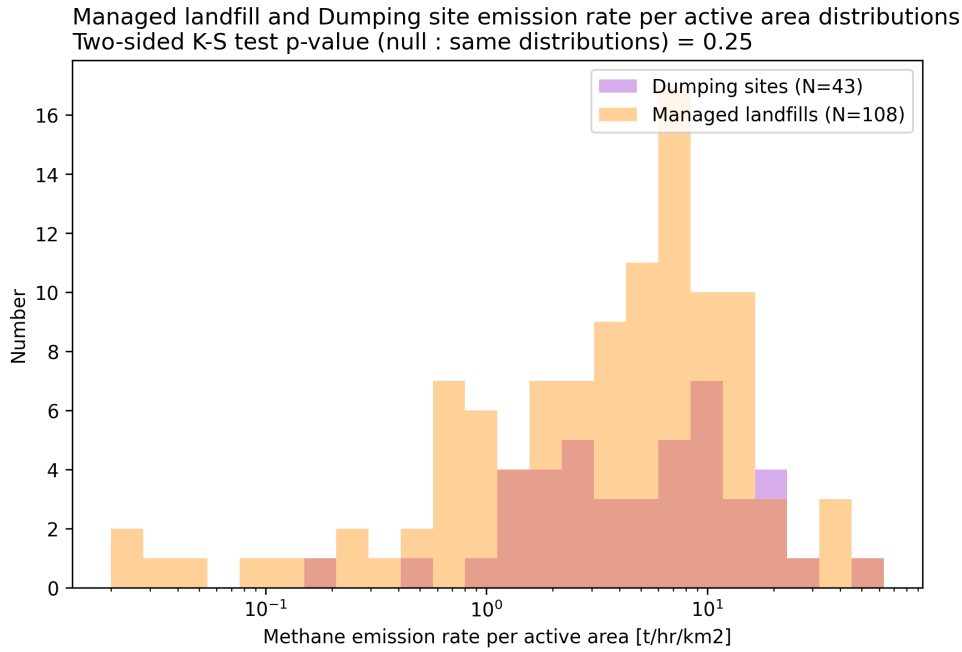

Figure S6.2. Distribution of emission rate per area for managed landfills and dumping sites considering the total site area (top) and the total Sentinel-2 detected surface activity area (bottom).

Supplement S7: site-wise reported or calculated dataset filters

This supplement provides data source references and filtering for reported and calculated facility-scale methane emissions.

Tables S7.1 to S7.4 report the data fields and values chosen to filter GHG emission reporting or calculation datasets.

US GHG Reporting program file names:

- 2022_data_summary_spreadsheets_0.zip, considering both files hereafter, and then computing either the mean, or using data from just one year depending on when GHGSat data have been observed:
  - ghgp_data_2021.xlsx
  - ghgp_data_2022.xlsx

US GHG Reporting program download link:

- (last accessed 2024-03-28) https://www.epa.gov/ghgreporting/data-sets

Data fields	Selected values
“Industry Type (subparts)”	'C,D,HH', 'C,DD,HH', 'C,HH', 'C,HH,TT', 'HH'

Table S7.1. Data fields and selected values used to select data from the US GHG Reporting.

The analysis is performed using the following data field that reports a yearly total in t of CO2e:

- ‘Methane (CH4) emissions ’

This total is converted to hourly rates assuming constant emissions, and using the AR4 CH4 GWP, as used by EPA (https://www.epa.gov/ghgreporting/ghgrp-reported-data, last accessed 2024-06-24).

Canadian GHG Reporting program file name:

- PDGES-GHGRP-GHGEmissionsGES-2004-Present.csv

Canadian GHG Reporting program download link:

- (last accessed 2024-06-06) https://open.canada.ca/data/en/dataset/a8ba14b7-7f23-462a-bdbb-83b0ef629823

Data fields	Selected values
"English Facility NAICS Code Description / Description du code SCIAN de l'installation en anglais"	'Waste Treatment and Disposal' OR 'Waste Collection' OR 'All Other Waste Management Services'
"Reference Year / Année de référence"	Considering both available values listed hereafter, and computing the mean, or using data from just one year depending on when GHGSat data have been observed: • 2021 • 2022

Table S7.2. Data fields and selected values used to select data from the Canadian GHG reporting program.

The analysis is performed using the following data field that reports a yearly total in metric tons of CH_4:

- 'CH4 (tonnes)'

This total is converted to hourly rates assuming constant emissions.

European GHG Reporting program (E-PRTR) file name:

- F1_4_Detailed releases at facility level with E-PRTR Sector and Annex I Activity detail into Air.xlsx

European GHG Reporting program download link:

- (last accessed 2024-06-06) https://sdi.eea.europa.eu/data/63a14e09-d1f5-490d-80cf-6921e4e69551?path=%2FUser%20friendly%20Excel%20file

Data fields	Selected values
'targetRelease'	'AIR'
'pollutant'	'Methane (CH4)'
Considering both values hereafter and then computing the mean, or using data from just one year depending on when GHGSat data have been observed: '2021' '2022'	>0

Table S7.3. Data fields and selected values used to select data from the European GHG reporting program (E-PRTR).

The analysis is performed using the following data fields that report a yearly total in kg of CH_4:

- '2021' and/or '2022'

This total is converted to hourly rates assuming constant emissions.

ClimateTRACE GHG emission calculation file name:

- solid-waste-disposal_emissions-sources.csv

ClimateTRACE GHG emission calculation:

- https://climatetrace.org/data

Data fields	Selected values
gas	Ch4
'start_time'	Considering both available values listed hereafter, and computing the mean, or using data from just one year depending on when GHGSat data have been observed:

	• '2021-01-01 00:00:00' • '2022-01-01 00:00:00'

Table S7.4. Data fields and selected values used to select data provided by ClimateTRACE.

The analysis is performed using the following data field that reports a yearly total in metric tons of CH_4:

- 'emissions_quantity'

This total is converted to hourly rates assuming constant emissions.

Supplement S8: Supplementary results for GHGSat comparison to facility-scale reported and calculated emission rates

This supplement provides the spatial distribution of the facilities for which we compare GHGSat-based results against reported (Figure S8.1, top) and Climate TRACE calculated emissions (Figure S8.1, bottom), along with difference statistics for all these comparisons (Tables S8.1 and S8.2).

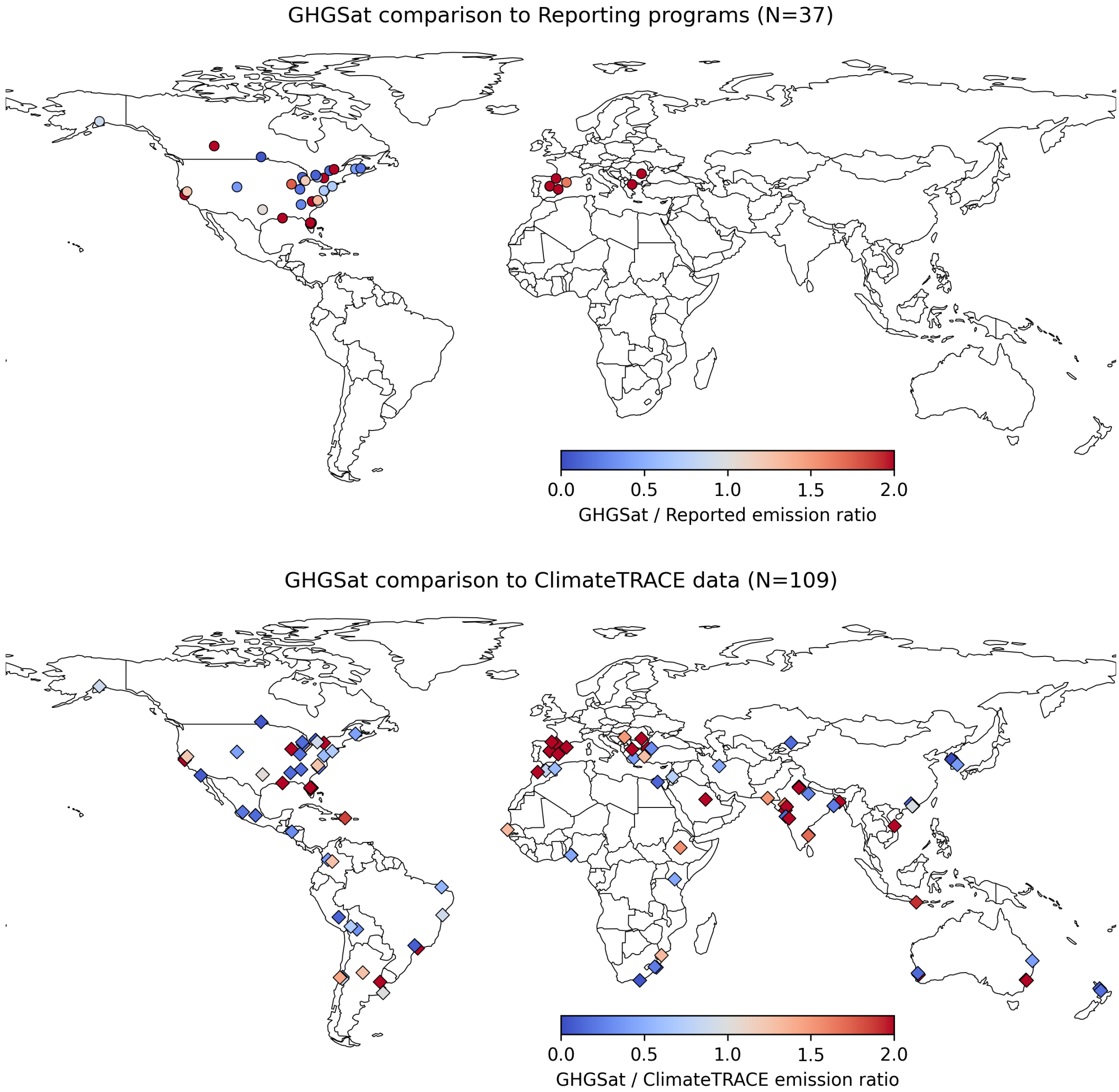

Figure S8.1. Spatial distribution of site-wise comparison between GHGSat methane emission rates and reported (top) or calculated (bottom, Climate TRACE) emissions.

Reporting scope	Number of sites	GHGSat – reported difference
USA	22	0.43 ± 1.45 t/hr
Canada	8	-0.49 ± 0.93 t/hr
EU	7	1.75 ± 1.22 t/hr
All together	37	0.48 ± 1.49 t/hr

Table S8.1. Methane emission rate difference statistics between GHGSat-based rates and data included in facility-scale reporting program databases.

Waste disposal site types	Number of sites	GHGSat – ClimateTRACE difference
Managed landfills	77	-0.63 ± 4.93 t/hr
Dumping sites	32	-0.35 ± 2.93 t/hr
All together	109	-0.55 ± 4.44 t/hr

Table S8.2. Methane emission rate difference statistics between GHGSat-based rates and data calculated by Climate TRACE.

Supplement S9: Analyzing the impact of reporting method choice for US facilities

The US Greenhouse Gas Reporting Program (GHGRP) requires that landfills provide annual methane emission estimates using two different methods: (1) based on gas capture efficiency; and (2) based on waste-decay modelling. Only one result is chosen by facility operators to be included in GHGRP data, but both are available on the 'Facility Level Information on GreenHouse gases Tool' (FLIGHT, https://ghgdata.epa.gov/ghgp/main.do) platform, run by the US Environmental Protection Agency (EPA). Using identified facilities in the US, this supplement examines the reporting method impact on how GHGSat-based results compare to bottom-up estimates.

Figure S9.1 provides a comparison of GHGSat-based emission rates against official GHGRP facility-scale reported data (top left), and against data computed with the method based on gas capture efficiency (bottom left) and based on waste decay modelling (bottom right). Regardless of the reported data, all three comparisons in Figure S9.1 exhibit low correlations between GHGSat-based emission estimates and reported data. The capture-based method leads to underestimating facility-scale emissions compared to GHGSat-based results, while waste-decay modelling appears to overestimate them. Both methods show a large scatter in how they compare to GHGSat.

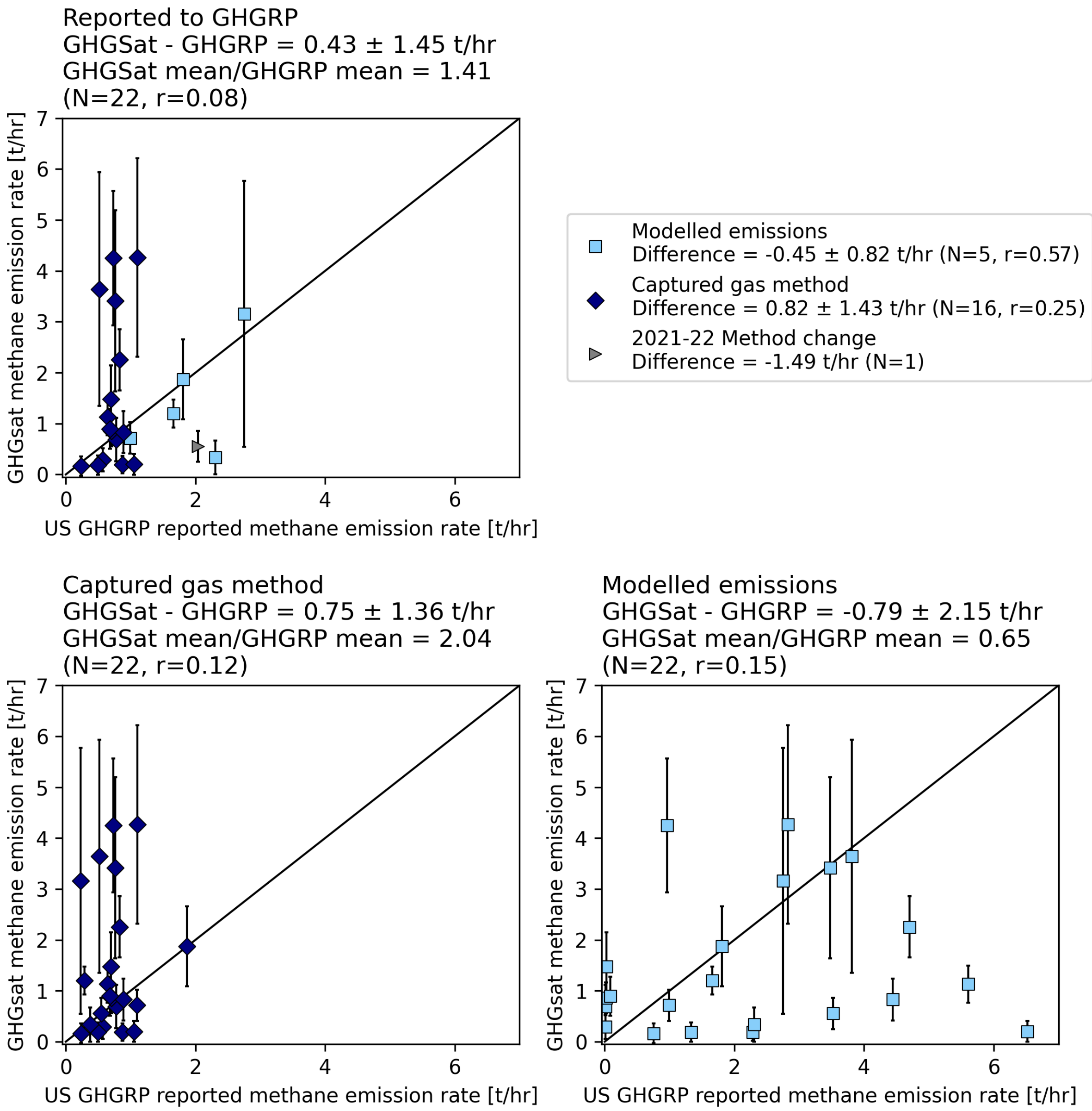

Figure S9.1. GHGSat-based emission rates compared to annual US GHGRP reported emissions rates averaged over the corresponding GHGSat observation years, and obtained from the official dataset (top left), the gas-capture efficiency method only (bottom left), and the waste-decay modelling (bottom right). Reported data are provided as annual totals and have been converted to hourly rates assuming constant emissions. Black lines show the 1:1 line.

Supplement S10: collected UNFCCC, UN WPP, and World Bank data

This supplement provides the basic information and data used to compare GHGSat-based results against UNFCCC reports for solid waste methane emissions at country scale. Table S10.1 provides collected UNFCCC data[6]. Table S10.2 provides collected population data from UN World Population Prospects (UN WPP) datasets[7–9], and Table S10.3 provides distance data collected or computed from the What a Waste World Bank report[10] along with computed population counts corresponding to these distances.

Country	**Annex**	**UNFCCC emission source**	**UNFCCC ref. year**	**UNFCCC ref. emissions**	**UNFCCC emissions scaled to 2022**
Units	**-**	**-**	**-**	**kt/yr**	**kt/yr**
Argentina	non-Annex I	BUR	2018	459	470.61
Australia	Annex I	Query	2020	340.41	347.12
Bangladesh	non-Annex I	NC	2012	97	109.24
Bolivia	non-Annex I	NC	2008	51.14	63.35
Brazil	non-Annex I	NC	2016	1857.19	1934.72
Canada	Annex I	Query	2021	717.37	722.75
Chile	non-Annex I	BUR	2020	233.88	238.07
China	non-Annex I	Query	2014	3842	3961.52
Colombia	non-Annex I	BUR	2018	379.89	401.54
Dominican Republic	non-Annex I	BUR	2015	182.15	196.67
Ecuador	non-Annex I	NC	2018	66	70.02
Egypt	non-Annex I	BUR	2015	632.48	719.42
Ethiopia	non-Annex I	NC	2018	14.46	16.06
Greece	Annex I	Query	2021	149.38	148.44
Honduras	non-Annex I	Query	2015	4.76	5.35
India	non-Annex I	Query	2016	754	799.26
Indonesia	non-Annex I	BUR	2019	1925.29	1968.94
Iran	non-Annex I	NC	2010	23	27.07
Israel	non-Annex I	Query	2020	269.91	278.67
Italy	Annex I	Query	2021	559.78	557.68
Jordan	non-Annex I	NC	2017	180.59	200.46
Kenya	non-Annex I	Query	2010	13.21	17.22
Kyrgyzstan	non-Annex I	BUR	2018	15.55	16.57
Malaysia	non-Annex I	BUR	2019	480	496.74
Mexico	non-Annex I	BUR	2019	1036.75	1057.02
Morocco	non-Annex I	NC	2018	133.24	138.93
Mozambique	non-Annex I	-	-	-	-
New Zealand	Annex I	Query	2021	103.13	104.37
Nigeria	non-Annex I	BUR	2017	281.93	318.53
Pakistan	non-Annex I	BUR	2018	487.14	522.34
Paraguay	non-Annex I	NC	2019	32.79	34.07
Peru	non-Annex I	BUR	2019	231.15	240.26
Romania	Annex I	Query	2021	155.47	156.26
Russia	Annex I	Query	2021	2802.88	2791.98
Saudi Arabia	non-Annex I	NC	2016	531.78	580.35

Senegal	non-Annex I	Query	2005	36.16	57.06
Serbia	non-Annex I	NC	2014	79.57	76.32
South Africa	non-Annex I	BUR	2017	826.95	875.19
South Korea	non-Annex I	Query	2018	373.03	374.34
Spain	Annex I	Query	2021	370.63	371.61
Thailand	non-Annex I	BUR	2019	333.73	335.61
Trinidad and Tobago	non-Annex I	BUR	2018	78.54	80.43
Tunisia	non-Annex I	BUR	2021	118.7	119.6
Turkey	Annex I	Query	2021	373.51	376.15
United States	Annex I	Query	2021	4379.06	4393.99
Uzbekistan	non-Annex I	BUR	2017	86.84	94.12
Vietnam	non-Annex I	BUR	2016	372.82	393.36

Table S10.1. Collected UNFCCC data for solid waste methane emissions.

Country	**Emission ref. year**	**2022 UN WPP total population for ref. year**	**2022 UN WPP total population for 2022**	**2015 UN WPP total population for 2020**
Units	**-**	**millions**	**millions**	**millions**
Argentina	2018	44.33	45.45	45.52
Australia	2020	25.61	26.11	25.6
Bangladesh	2012	151.61	170.74	170.47
Bolivia	2008	9.84	12.19	11.55
Brazil	2016	206.45	215.07	216
Canada	2021	38.09	38.37	37.6
Chile	2020	19.25	19.6	18.84
China	2014	1382.89	1425.91	1411.04
Colombia	2018	49.04	51.83	50.23
Dominican Republic	2015	10.38	11.2	11.11
Ecuador	2018	16.92	17.95	17.34
Egypt	2015	97.2	110.56	100.52
Ethiopia	2018	110.39	122.6	111.97
Greece	2021	10.46	10.4	10.83
Honduras	2015	9.25	10.39	8.65
India	2016	1334.63	1414.75	1388.86
Indonesia	2019	268.96	275.06	271.86
Iran	2010	75.1	88.4	83.4
Israel	2020	8.72	9	8.72
Italy	2021	59.3	59.08	59.74
Jordan	2017	10.15	11.27	8.17
Kenya	2010	41.23	53.76	52.19
Kyrgyzstan	2018	6.2	6.6	6.38
Malaysia	2019	32.7	33.84	32.37
Mexico	2019	124.82	127.26	134.84
Morocco	2018	35.83	37.36	36.44
Mozambique	1990	13.24	32.74	31.99
New Zealand	2021	5.11	5.17	4.73

Nigeria	2017	192.27	217.23	206.83
Pakistan	2018	218.86	234.67	208.44
Paraguay	2019	6.51	6.76	7.07
Peru	2019	32.69	33.98	33.32
Romania	2021	19.36	19.46	18.85
Russia	2021	145.29	144.72	142.9
Saudi Arabia	2016	33.24	36.27	34.37
Senegal	2005	10.9	17.21	17.49
Serbia	2014	7.55	7.24	8.67
South Africa	2017	56.48	59.77	56.67
South Korea	2018	51.64	51.82	51.25
Spain	2021	47.44	47.57	46.19
Thailand	2019	71.27	71.67	68.58
Trinidad and Tobago	2018	1.49	1.53	1.38
Tunisia	2021	12.24	12.33	11.84
Turkey	2021	84.62	85.22	82.26
United States	2021	336.75	337.89	337.62
Uzbekistan	2017	31.82	34.49	31.77
Vietnam	2016	92.9	98.01	98.16

Table S10.2. Collected UN WPP population data.

Country	**Minimum population integration distance (r_{min})**	**Population within r_{min} from GHGSat targets**	**Reference population integration distance (r)**	**Population within r from GHGSat targets**	**Maximum population integration distance (r_{max})**	**Population within r_{max} from GHGSat targets**
Units	**km**	**millions**	**km**	**millions**	**km**	**millions**
Argentina	40	16.71	60	19.8	80	20.88
Australia	20	3.42	40	8.8	50	9.8
Bangladesh	20	20.12	40	31.37	50	36.25
Bolivia	20	1.85	40	2.94	50	3.24
Brazil	20	28.21	40	47.51	50	53.94
Canada	20	4.65	40	13.23	50	15.21
Chile	20	3.78	40	8.93	50	9.4
China	20	18.68	40	54.25	50	76.42
Colombia	100	15.61	120	17.02	140	20.74
Dominican Republic	20	4.34	40	5.92	50	6.27
Ecuador	20	0.95	40	2.52	50	3.09
Egypt	20	9.1	40	29.69	50	33.9
Ethiopia	20	4.01	40	4.98	60	6.4
Greece	80	7	100	7.53	120	7.91
Honduras	20	0.94	40	1.43	50	1.59
India	20	98.79	40	148.61	50	171.83
Indonesia	60	1.7	80	2.25	100	2.68
Iran	60	13.64	80	15.76	100	17.29
Israel	60	2.28	80	4.22	100	6.06
Italy	20	2.29	40	4.06	50	4.65
Jordan	30	3.55	50	5.07	70	6.2

Kenya	20	5.15	40	6.98	50	7.67
Kyrgyzstan	20	1.15	40	1.38	50	1.5
Malaysia	20	0.36	40	3.95	50	6.52
Mexico	20	15.43	40	28.71	60	32.54
Morocco	20	8.72	40	12.58	50	13.91
Mozambique	20	2.19	40	2.65	50	2.72
New Zealand	20	0.62	40	2.06	50	2.43
Nigeria	20	13.51	40	17.23	50	18.04
Pakistan	30	18.14	50	24.76	70	31.31
Paraguay	20	1.84	40	2.79	50	2.9
Peru	20	0.53	40	0.67	50	0.73
Romania	20	1.57	40	3.38	50	4.63
Russia	50	14.06	70	19.25	90	20.63
Saudi Arabia	60	4.2	80	5	100	5.16
Senegal	20	6.96	40	9.73	50	10.06
Serbia	20	1.35	40	1.99	50	2.19
South Africa	20	2.73	40	4.29	50	4.44
South Korea	110	44.14	130	48.71	150	50.07
Spain	20	5.74	40	15.77	50	19.37
Thailand	20	0.38	40	1.47	50	2.63
Trinidad and Tobago	20	0.37	40	1.22	50	1.6
Tunisia	40	2.77	50	3.15	70	4.11
Turkey	20	3.74	40	10.14	50	12.36
United States	20	11.87	40	35.84	50	47.36
Uzbekistan	20	1.13	40	3.21	50	3.55
Vietnam	50	36.89	70	46.8	80	50.74

Table S10.3. Distance between city center and major waste disposal sites computed from the What a Waste World Bank report (reference, lower and upper boundaries), and total population residing within these distances from GHGSat targets in each country.

UNFCCC data URLs:

- Flexible queries Annex-I: https://di.unfccc.int/flex_annex1
- Flexible queries non-Annex-I: https://di.unfccc.int/flex_non_annex1
- Biennial Update Reports (BUR): https://unfccc.int/BURs
- National Communications (NC): https://unfccc.int/non-annex-I-NCs

Figure S10.1 shows the distribution of the distance between city center and main waste disposal site collected from the 'What a Waste' World Bank report dataset that covers 125 cities worldwide, but not all countries[10]. This distribution shows a global average of 17.7 km, and this value is employed in our study unless the dataset includes data for a considered country.

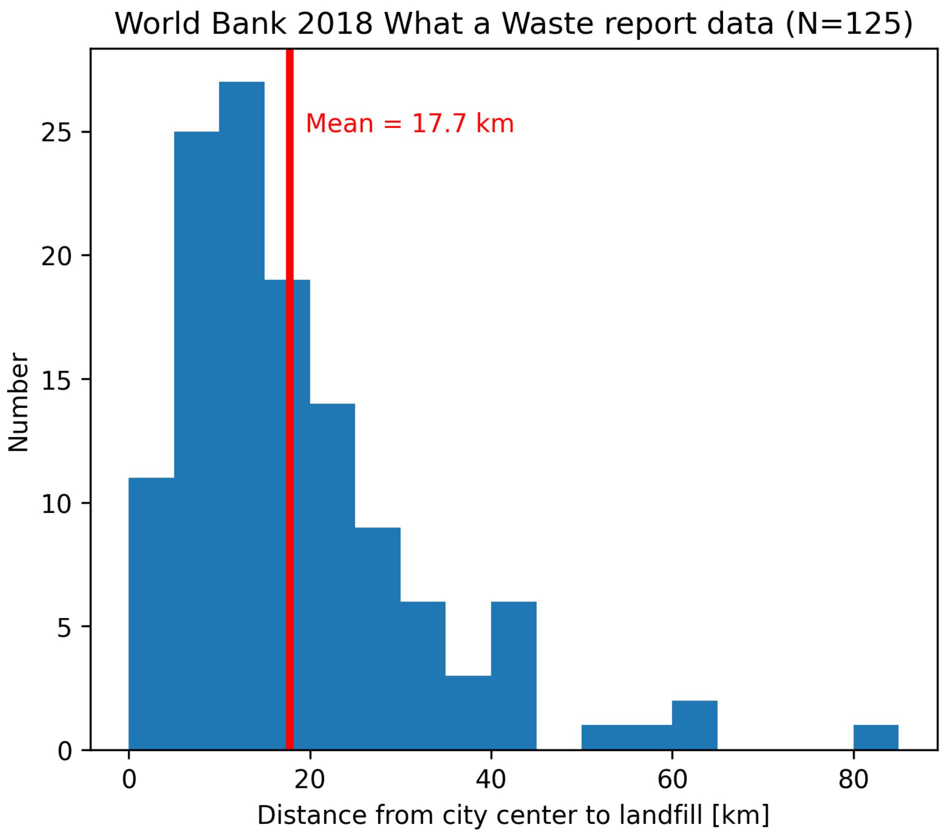

Figure S10.1. Distribution of distances from the city center to the main waste disposal site reported for 125 cities by the World Bank in the 2018 What a Waste report.

Supplement S11: Supplementary visuals and data for GHGSat comparison to country-scale UNFCCC data

This supplement provides the GHGSat against UNFCCC emission per capita comparison results at country and global scales. Figure S11.1 shows the spatial distribution of this comparison. Uncertainty bars on GHGSat-based emissions per capita include two uncertainty sources: (1) uncertainties on GHGSat emissions; and (2) uncertainties on population scaling of those emissions (summed within r_{min} to r_{max} from country-wise GHGSat targets), which is the largest contributor to the overall uncertainty. To illustrate where most of the uncertainty on GHGSat-based emission per capita comes from, Figures S11.2 and S11.3 replicate the inset scatter plot included in Figure S11.1 with and without the contribution of population uncertainty on the GHGSat emission per capita uncertainty. While uncertainties on UNFCCC emissions are reported, we have not included them here as they are complicated to inventory across the data sources used and conversion into per capita estimates is difficult.

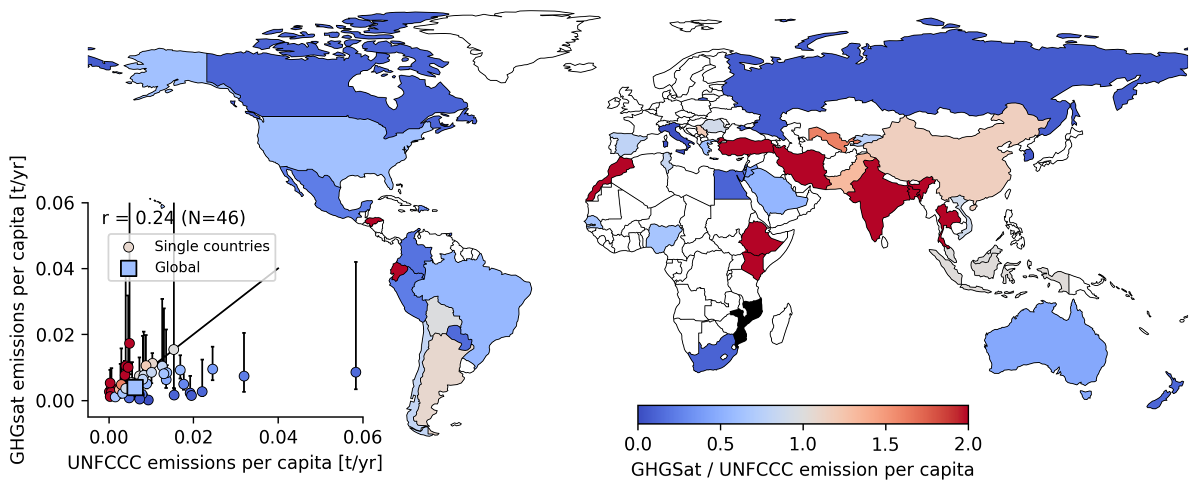

Figure S11.1. Comparison of GHGSat-based and UNFCCC-based solid waste methane emissions per capita. The color shows the ratio between GHGSat and UNFCCC based results. Error bars included in the scatter plot include the contributions of both GHGSat observation uncertainties and population uncertainties. Mozambique is colored in black as no solid waste methane emission has been found for this country in UNFCCC datasets. Borders are taken from Natural Earth (https://www.naturalearthdata.com/about/map-update-committee/) that provides *de facto* administrative boundaries.

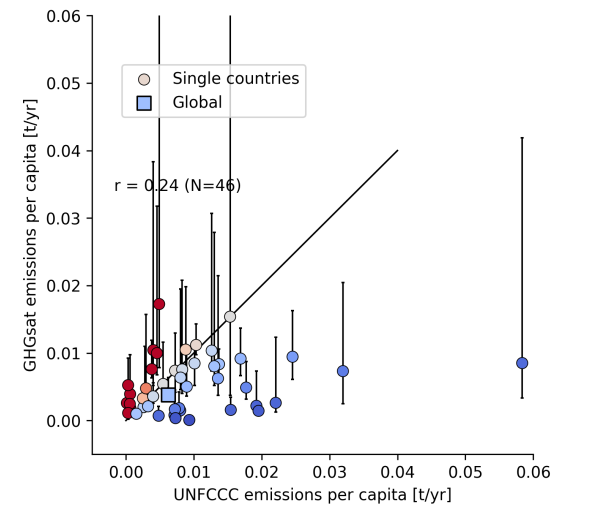

Figure S11.2. Reproduction of the scatter included in Figure S11.1, including uncertainty on population.

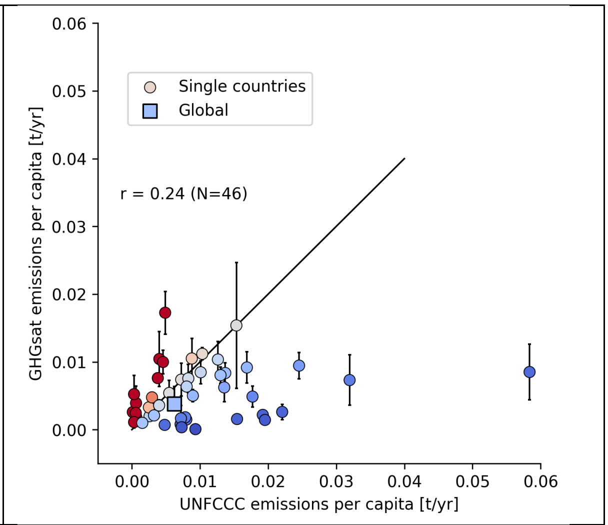

Figure S11.3. Reproduction of the scatter included in Figure S11.1, ***excluding*** uncertainty on population.

To better describe the coverage of the GHGSat archive dataset considered here, we provide the number of waste disposal sites observed in each country in Figure S11.4. Overall, we have a median coverage of 2 sites per country, with a maximum of 23 sites in the US. Finally, we provide the maximum population fraction covered by GHGSat targets in Figure S11.5. The population values underlying these fractions in Figure S11.5 relate to the lower-ends of the vertical uncertainty bars included in Figures S11.1 and S11.2. Overall, we have a median country-wise maximum estimated population coverage of 24%, with a minimum of 1% in Indonesia, and a maximum of 98% in South Korea.

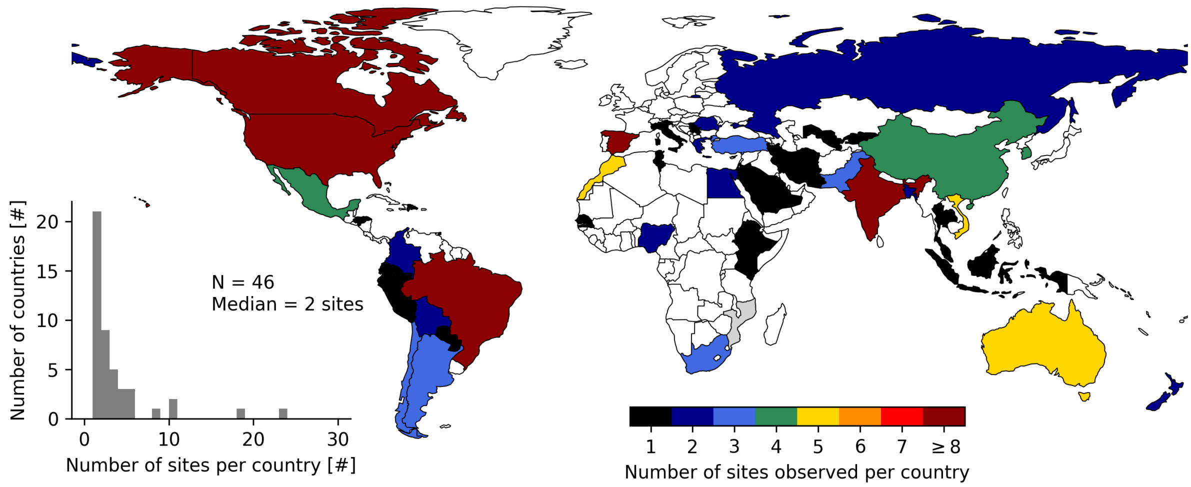

Figure S11.4. Distribution of the number of waste disposal sites observed per country in this GHGSat archive dataset. Mozambique is colored in grey as no solid waste methane emission has been found for this country in UNFCCC datasets. Borders are taken from Natural Earth (https://www.naturalearthdata.com/about/map-update-committee/) that provides *de facto* administrative boundaries.

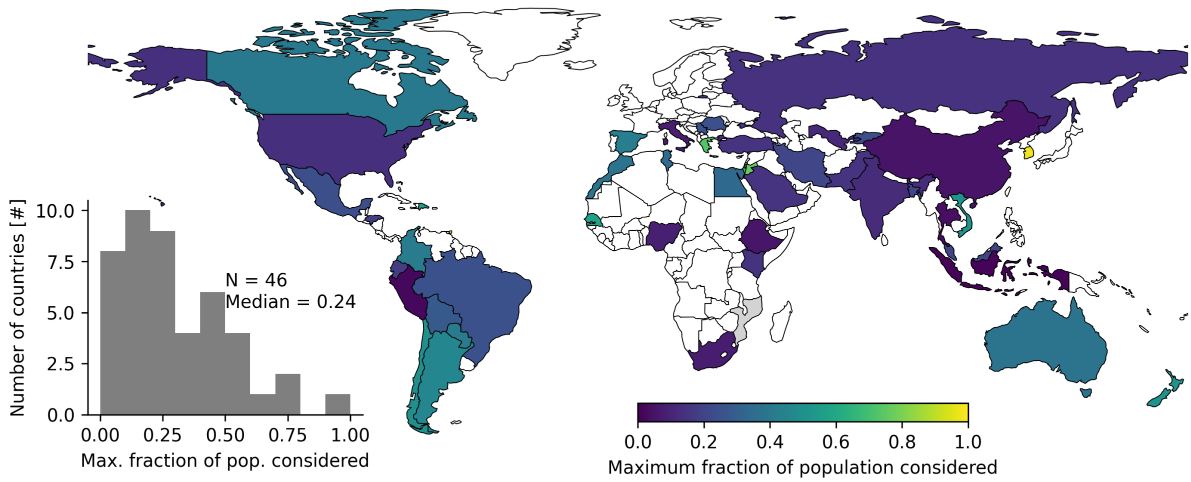

Figure S11.5. Distribution of the maximum country-wise population fraction considered for the calculation of emissions per capita. This population fraction corresponds to the lower end of the vertical uncertainty bars included in Figures S11.1 and S11.2. Mozambique is colored in grey as no solid waste methane emission has been found for this country in UNFCCC datasets. Borders are taken from Natural Earth (https://www.naturalearthdata.com/about/map-update-committee/) that provides *de facto* administrative boundaries.

Supplement S12: Surface activity detection in waste disposal sites from Sentinel-2 clear sky image timeseries

This supplement describes the algorithm developed for surface activity detection in Sentinel-2 RGB imagery data.

Waste disposal site masks

We outline waste disposal site boundaries using the latest available Google Earth imagery and conduct all the following surface activity analysis within the obtained boundaries, hereafter called "site masks". We also use these boundaries to calculate A, the site area.

Data download

We download Sentinel-2 RGB imagery at 10-m resolution from the Google Earth Engine "COPERNICUS/S2_SR_HARMONIZED" collection in 0.04°x0.04° square images centered on each landfill location, and only include images that show:

- CLOUDY_PIXEL_PERCENTAGE lower than 1%
- A percentage of medium and high probability of cloudy pixels (Surface Classification (SCL) types equal to 8 and 9) within the landfill mask of less than 5%

For each site, the images we use are comprised within 60 days before the first GHGSat observation and 60 days after the last GHGSat observation. In total, we could download Sentinel-2 data that pass these criteria for 119 sites of the 151 observed by GHGSat.

Additional water pixel masking

For each timestamp t, we compute the 5th reflectance percentile in the 12th band (B12) of Sentinel-2 (around 2.2 µm) for all the pixels contained in the site mask. If this 5th reflectance percentile is below 0.1, we preliminary mask all pixels with a B12 reflectance below this value as water pixels. We add a 5-pixel buffer around this preliminary mask to obtain the final water mask.

Additional cloudy pixel masking

For each timestamp t, we preliminary mask all pixels contained in the site mask with Scene Classification (SCL) types equal to 3 (cloud shadow), 8 (clouds medium probability), 9 (clouds high probability) and 10 (cirrus) as cloudy pixels. We add a 7-pixel buffer around this preliminary mask to obtain the final cloudy pixel mask.

Activity detection algorithm

The activity detection algorithm includes several steps, as illustrated in Figure S12.1.

1. We first convert each RGB image to Grayscale RGB (GRGB) by using the NTSC formula: GRGB = 0.299xR + 0.587xG + 0.114xB

2. For a given timestamp t (panels a', b', e, f, g and h in Figure S12.1), we yield the two local Structural SIMilarity maps (SSIM) obtained between images at timestamps t-1 and t (c), and images at timestamps t and t+1 (c').

For both local SSIM maps, we select as most dissimilar the pixels for which SSIM are below or equal to a given percentile P of their respective SSIM distributions (d, d'). We just consider pixels within site boundaries, and exclude pixels additionally masked as water in images at timestamps t-1 and t, and t and t+1, respectively. We use as empirically determined percentile thresholds:

- $P = 5$, if the landfill area $A > 1$ km^2
- $P = 7.5$, if the landfill area $A \leq 1$ km^2

3. We obtain surface activity for timestamp t (e) as the intersection of most dissimilar pixels selected from local SSIM maps obtained between timestamps t-1 and t (c, d) and timestamps t and t+1 (c', d')

4. This three-timestamp moving-window does not allow to obtain activity for the first and last images at timestamps t0 and tmax, respectively.

   Surface activity for the first image at timestamp t0 is identified as the dissimilar pixels selected in the local SSIM map between timestamps t0 and t0+1 that are not included in activity detected for timestamp t0+1.

   Surface activity for the last image at timestamp tmax is identified as the dissimilar pixels selected in the local SSIM map between timestamps tmax-1 and tmax that are not included in activity detected for the timestamp tmax-1.

5. For each timestamp t, we mask out pixels associated with water and clouds (see descriptions of additional water and cloud masking, panel f in Figure S12.1).

6. For each timestamp t, we smooth the remaining pixels associated with surface activity with a median filter using neighborhood sizes dependent on the site size:
   - 50x50 m^2, if the site area $A > 1$ km^2
   - 30x30 m^2, if the site area $A \leq 1$ km^2

   We then perform a binary dilation of the smooth binary activity map Nd times, with:
   - Nd = 5, if the site area $A > 1$ km^2
   - Nd = 3, if the site area $A \leq 1$ km^2

   The result of these two operations highlights spatially consistent activity within the site boundaries (panel g in Figure S12.1).

7. We finally identify individual activity clusters and delineate them with convex hulls, which are compared to GHGSat plume origins (panel h in Figure S12.1).

To ensure the surface activity detection quality, we examine results obtained for each site. We evaluate how the automatically detected surface activity matches what can be visually noticed in RGB and GRGB images. We exclude from the analysis sites where the metric poorly captures real surface activity. For example, those can be caused by:

- A small number of available Sentinel-2 images that result in large temporal gaps between images.
- Miss-classifications in the Sentinel-2 Surface Classification (SCL) product, wrongfully identifying pixels as cloudy or non-cloudy.

- Spurious snowy surfaces that do not compare well with non-snowy images.
- No significant surface activity, leading to insignificant features being identified as surface activity (due to the relative SSIM threshold we use).

Over the 119 sites with sufficient Sentinel-2 data, we keep 107 where we can capture surface activity. Some artefacts can remain in these results. For example, these can be associated with different turbid leachate water colors that challenge the additional water masking, or linked to small orthorectification errors that affect elevated features in sites that may not be resolved by the Digital Elevation Model used for orthorectification.

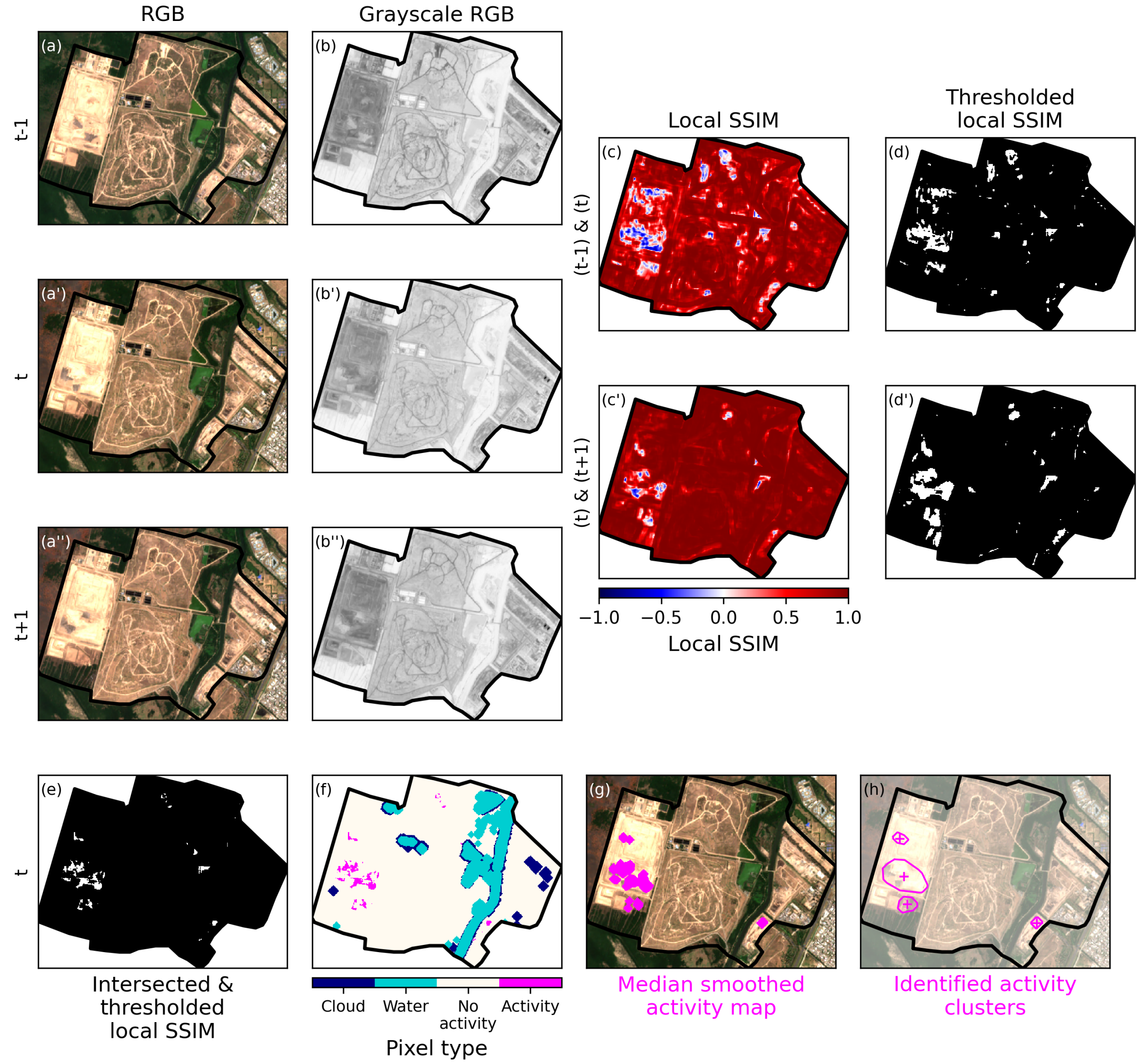

Figure S12.1. Illustration of the activity detection algorithm applied on Sentinel-2 imagery for Norte III landfill in Buenos Aires, Argentina. RGB images for timestamps t-1, t and t+1 (a, a', a'') are converted to Grayscale RGB images (b, b', b''). Local Structural SIMilarity (SSIM) maps are computed between timestamps t-1 and t (c) and t and t+1 (c'), and strongly dissimilar areas (low SSIM values) are selected by applying a threshold (d, d'). The overlap between these two images shows current activity at timestamp t (e). Pixels that are associated with water or clouds are removed from the analysis (f), and the resulting activity map is smoothed using a median filter and dilated back afterwards (g). Spatially consistent activity clusters remain and are outlined using convex hulls (h). All this analysis is performed within landfill boundaries, outlined by the thick black line in all panels.

Supplement S13: Comparison of GHGSat-based plume sources and Sentinel-2 detected surface activity

This supplement describes the metric and method used to evaluate the proximity between GHGSat-based plume sources and Sentinel-2 detected surface activity.

For all 107 waste disposal sites with sufficient Sentinel-2 data and adequate surface activity detection results, we compare the manually verified locations of GHGSat-detected plume sources with the closest in-time Sentinel-2 image for which surface activity has been detected. The comparison process and significance metric are illustrated in Figure S13.1.

For each GHGSat-detected plume source i, we compute its distance d_i to the spatially closest Sentinel-2 surface activity cluster detected in the temporally closest Sentinel-2 image (panels 1 – 14, dashed thin vertical lines in the bottom right panel of Figure S13.1). We then compute the averaged distance to the closest surface activity cluster across all site-wise sources $\bar{d} = \left(\frac{1}{N}\right)\sum_{i=1}^{N} d_i$ (dashed thick vertical line in the bottom right panel of Figure S13.1).

To evaluate the statistical significance of this averaged distance $\bar{d}$, for each distance d_i, we also compute the distance to the closest activity cluster d_i' distribution for 10000 points randomly drawn within the landfill mask (thin histogram lines in the bottom right panel of Figure S13.1). We then compute the distribution of similarly averaged distances to the closest surface activity cluster across all site-wise random sources $\bar{d}' = \left(\frac{1}{N}\right)\sum_{i=1}^{N} d_i{}'$ (thick black histogram line in the bottom right panel of Figure S13.1).

We finally compute the p-value, representing here the probability of obtaining averaged randomly drawn distances to the closest activity clusters smaller than what is obtained with GHGSat observations (probability of the null hypothesis yielding a result as extreme as the observations)

$$\text{p-value} = P\left(\bar{d}' \leq \bar{d}\right)$$

We consider that we find a statistically significant proximity between GHGSat plume sources and Sentinel-2 detected surface activity if p-value<0.05.

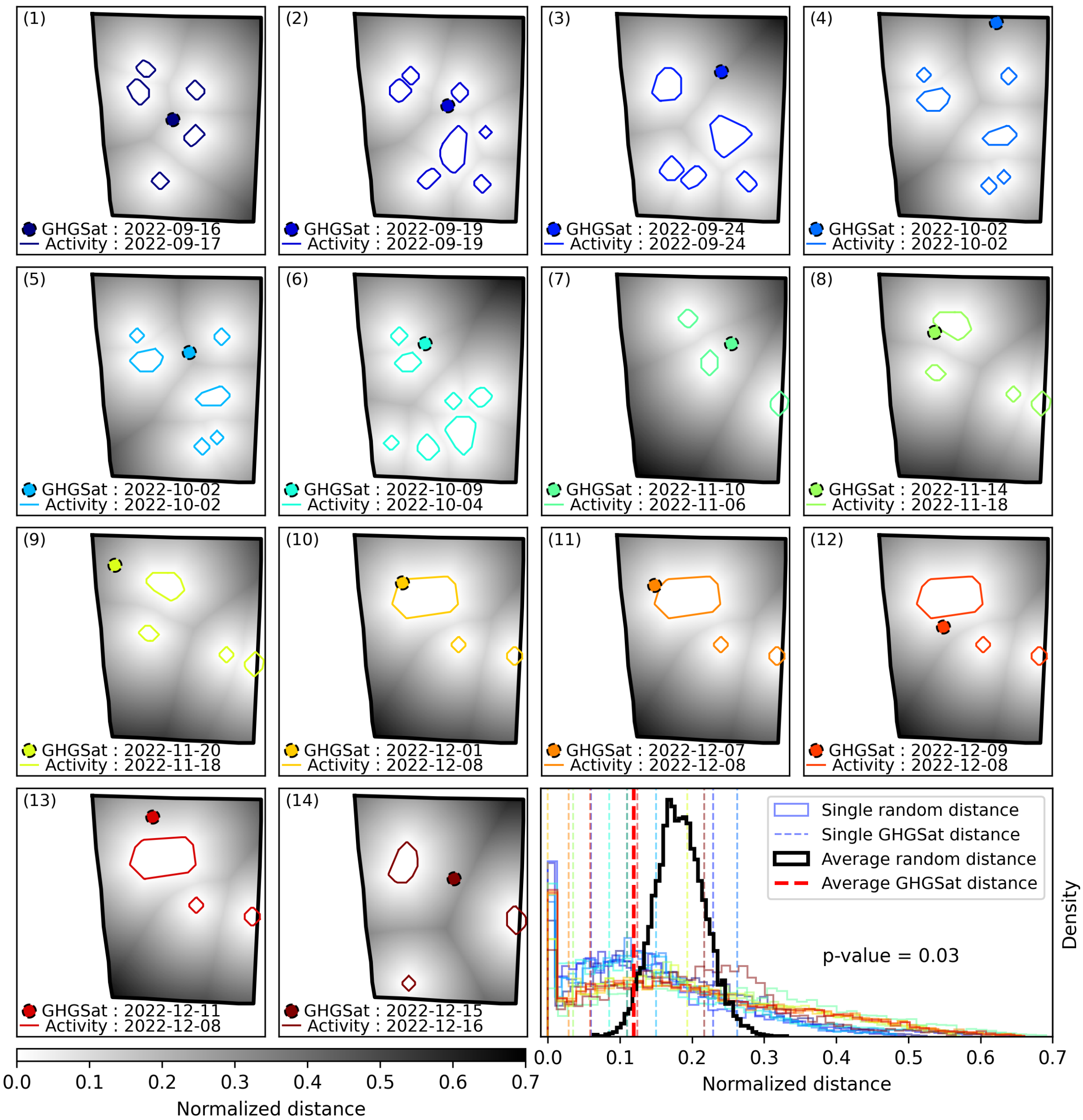

Figure S13.1. Illustration of the comparison between GHGSat-detected plume sources and Sentinel-2 detected landfill surface activity over the Amman landfill, Jordan. Comparison of GHGSat-detected plume origins (color-filled dashed circles) with closest-in-time Sentinel-2 detected surface activity (colored thin full-lines) and spatial distribution of the distance to closest activity cluster (panels 1 – 14). Single and averaged distances to the closest activity-cluster for GHGSat detected plume sources (thin and thick dashed lines) and single and averaged distance to the closest activity-cluster distributions for randomly drawn plume sources (full thin and thick histogram lines, bottom right panel). All distances are normalized by the square root of the landfill's area.

Supplement S14: Results of GHGSat plume sources comparison with Sentinel-2 detected surface activity

This supplement provides an overview of GHGSat plume sources comparison with Sentinel-2 detected surface activity, and illustrates results for a few sites in addition to the Casablanca landfill shown in Figure 2.

Figure S14.1 summarizes the results obtained for GHGSat plume source comparison to Sentinel-2 detected landfill surface activity over the 107 sites that passed all filtering criteria. We count 44/107 (41%) sites that show a statistically significant proximity (p-value<0.05) between GHGSat-detected plume sources and Sentinel-2 detected surface activity. The ratio of sites that show positive results increases when we restrict the analysis to sites where at least a given number of GHGSat-detected plume sources are available. For example, 18/21 (82%) sites that present at least 16 GHGSat-detected plume sources show statistically significant proximity (p-value<0.05). From these results, we conclude (1) that in many cases GHGSat-detected plumes are related to landfill surface activity; and (2) that increasing the number of observations over a given landfill helps to track emission sources within the facility, and more precisely pinpoint them if they are stationary.

Figures S14.2 to S14.6 illustrate site-wise comparisons between GHGSat-detected plume sources and Sentinel-2 detected surface activity for different sites, as shown in Figure 2 for Casablanca landfill.

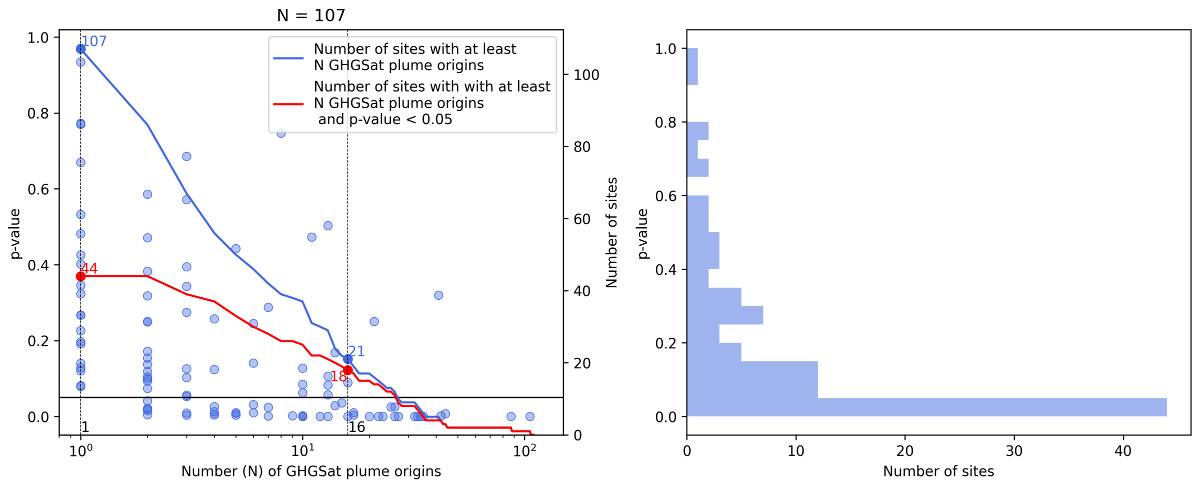

Figure S14.1. P-value for all 107 sites against the number of plume sources identified per site (left panel and y-axis) and total number of sites that show at least a given number of plume sources (blue line, left panel and right y-axis) and that also show a p-value < 0.05 (red line, left panel and right y-axis). Distribution of p-value values (right panel).

Site_ID = 4
Campo de Mayo
Buenos Aires
Argentina
Latitude, Longitude = -34.52769, -58.62434
Number of plume sources = 106, Number of S-2 activity clusters = 38
Mean distance p-value = 0.00, Manual S-2 activity results quality Label = 1

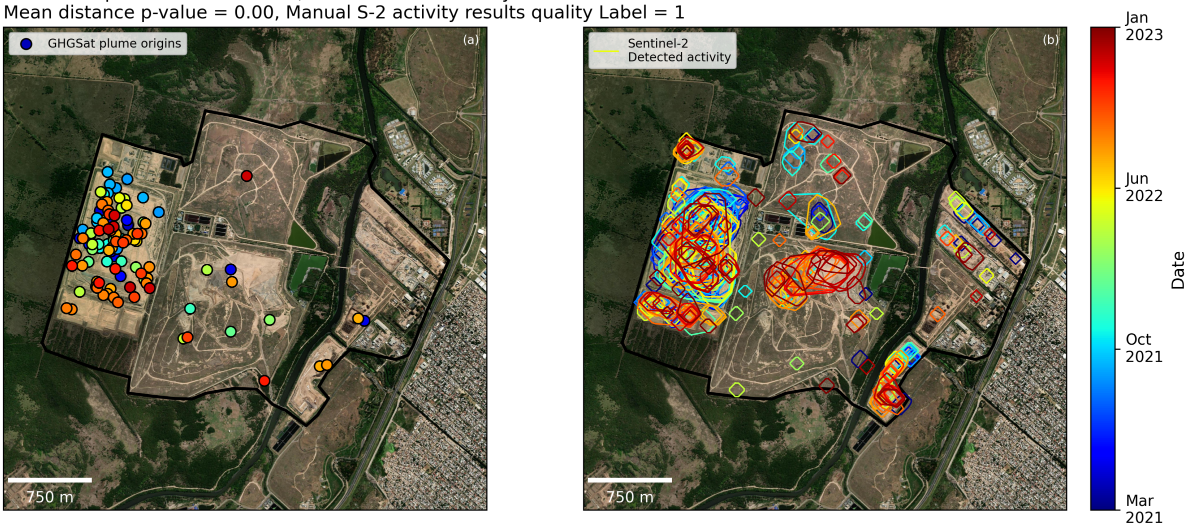

Figure S14.2. Comparison results for GHGSat-detected plume sources (left) and Sentinel-2 detected surface activity (right) at Norte III landfill, in Buenos Aires, Argentina. Background images are retrieved from Esri World Imagery[11].

Site_ID = 14
Cochabamba
Cochabamba
Bolivia
Latitude, Longitude = -17.47656, -66.12726
Number of plume sources = 10, Number of S-2 activity clusters = 23
Mean distance p-value = 0.00, Manual S-2 activity results quality Label = 1

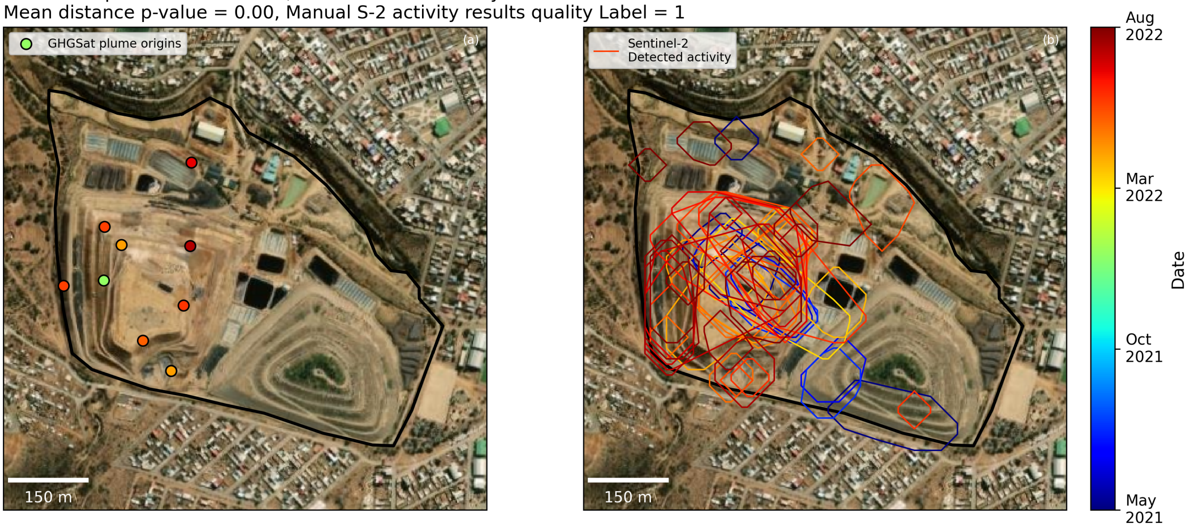

Figure S14.3. Comparison results for GHGSat-detected plume sources (left) and Sentinel-2 detected surface activity (right) at Cochabamba landfill, in Bolivia. Background images are retrieved from Esri World Imagery[11].

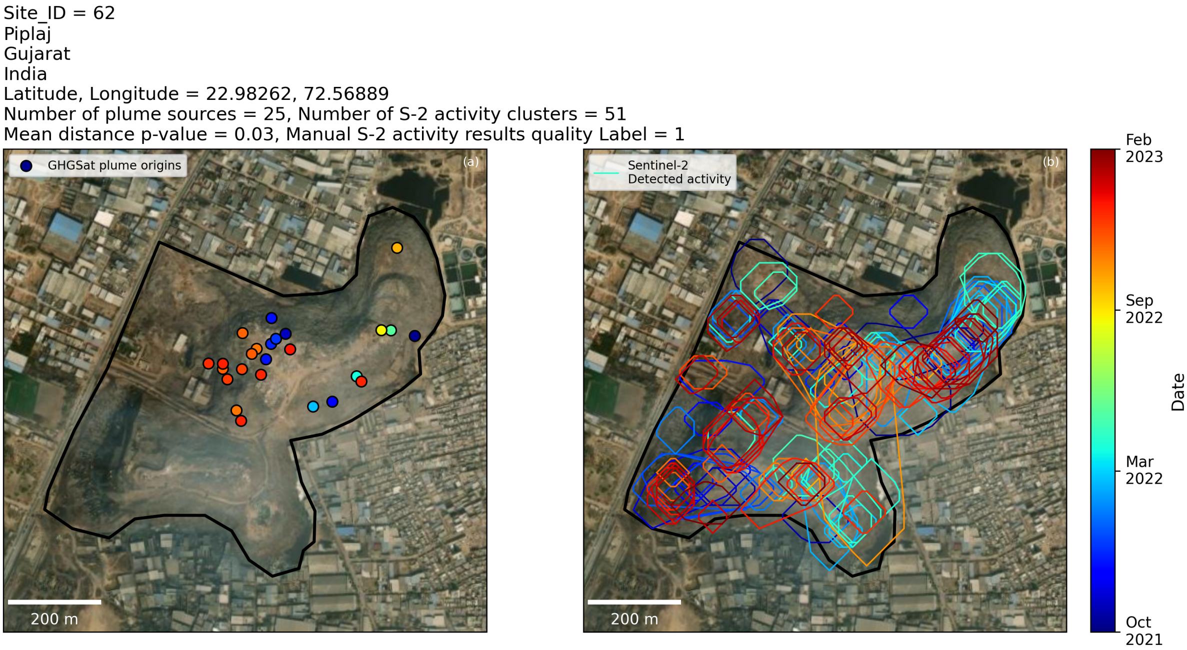

Figure S14.4. Comparison results for GHGSat-detected plume sources (left) and Sentinel-2 detected surface activity (right) at a landfill near Ahmedabad, in India. Background images are retrieved from Esri World Imagery[11].

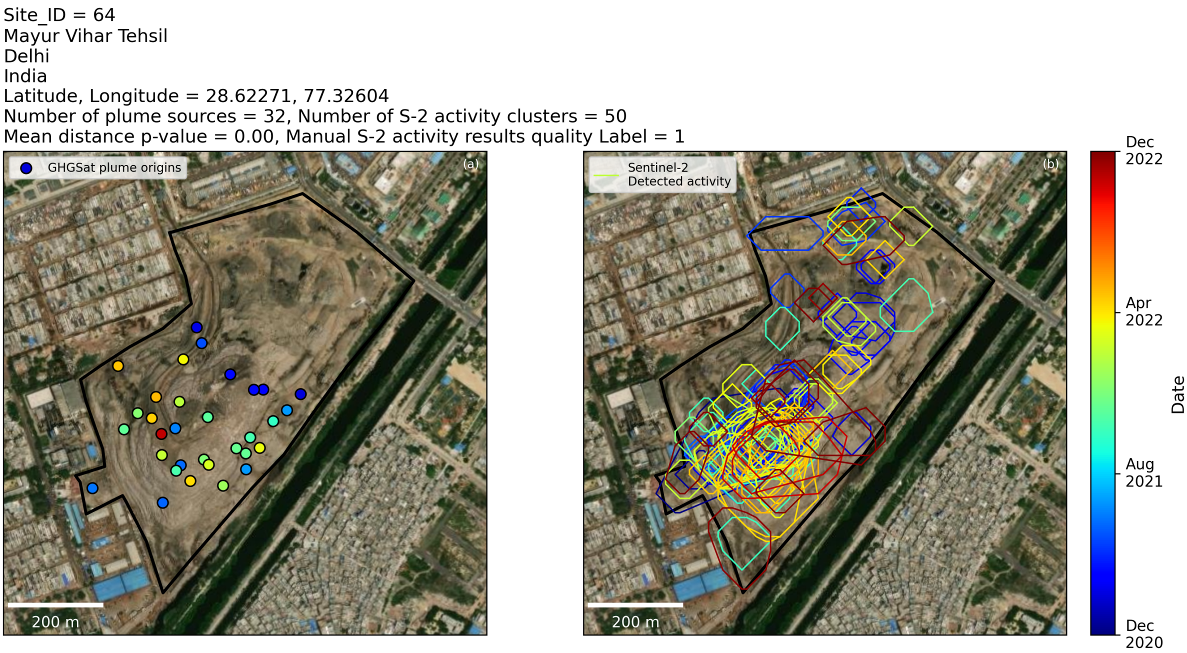

Figure S14.5. Comparison results for GHGSat-detected plume sources (left) and Sentinel-2 detected surface activity (right) at Ghazipur landfill, in Delhi, India. Background images are retrieved from Esri World Imagery[11].

Site_ID = 150
Nelson Mandela Bay Metropolitan Municipality
Eastern Cape
South Africa
Latitude, Longitude = -34.01751, 25.56686
Number of plume sources = 3, Number of S-2 activity clusters = 55
Mean distance p-value = 0.01, Manual S-2 activity results quality Label = 1

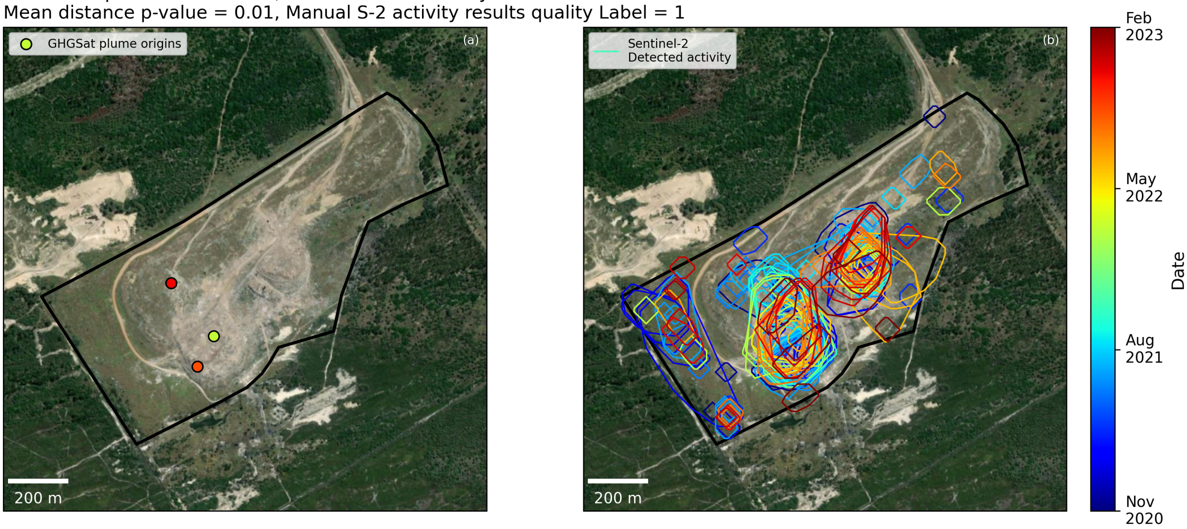

Figure S14.6. Comparison results for GHGSat-detected plume sources (left) and Sentinel-2 detected surface activity (right) at Nelson Mandela Bay Municipality landfill, in South Africa. Background images are retrieved from Esri World Imagery[11].

Supplement S15: example of detected plumes arising from other facilities than landfills

Figure S15.1 and S15.2 show methane emission plumes arising from a wastewater treatment plant in Shanghai and from a biogas plant in Madrid, respectively.

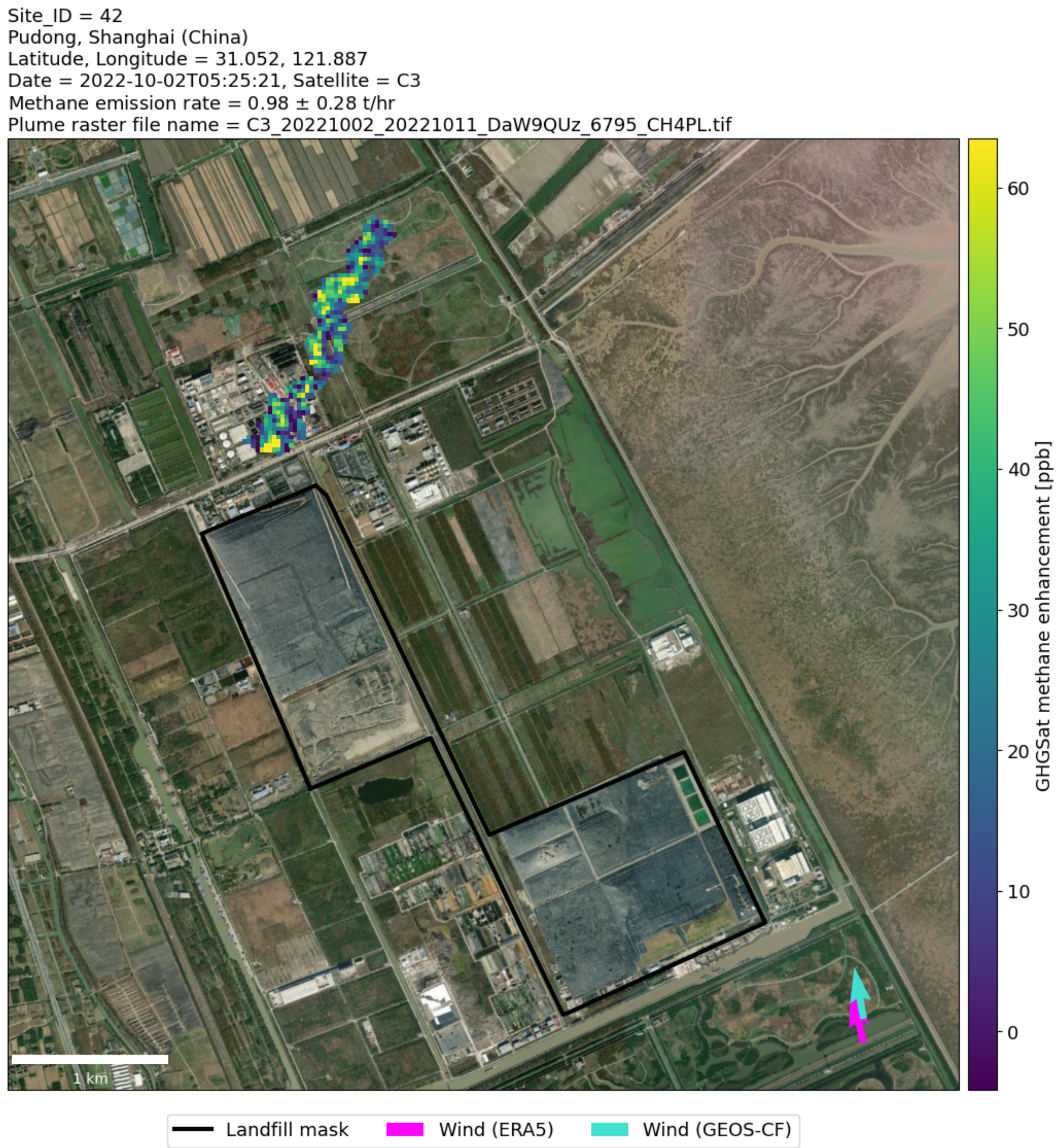

Figure S15.1 Methane emission plume arising from a wastewater treatment plant located close to the targeted landfill near Shanghai, and observed by GHGSat's C3 satellite on 2022 Oct 5th. Background images are retrieved from Esri World Imagery[11].

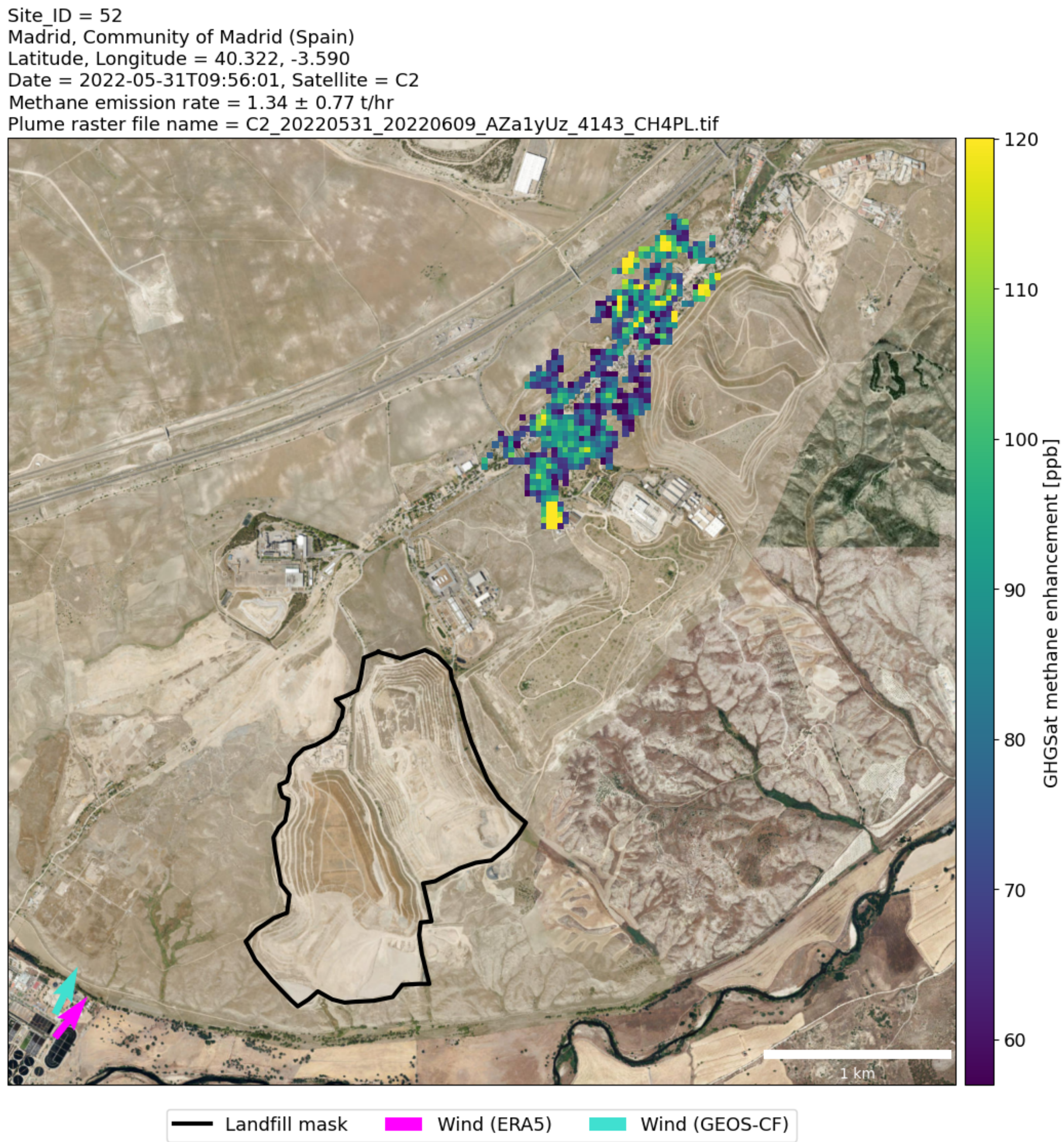

Figure S15.2 Methane emission plume arising from a biogas plant located close to a targeted landfill near Madrid, and observed by GHGSat's C2 satellite on 2022 May 31st. Background images are retrieved from Esri World Imagery[11].

References

1. Maasakkers, J. D. *et al.* Using satellites to uncover large methane emissions from landfills. *Sci. Adv.* **8**, eabn9683 (2022).
2. European Commission. EDGAR (Emissions Database for Global Atmospheric Research) Community GHG Database version 8.0. (2018).
3. Schuit, B. J. *et al.* Automated detection and monitoring of methane super-emitters using satellite data. *Atmospheric Chem. Phys.* **23**, 9071–9098 (2023).
4. Piano, S. L., Ferretti, F., Puy, A., Albrecht, D. & Saltelli, A. Variance-based sensitivity analysis: The quest for better estimators and designs between explorativity and economy. *Reliab. Eng. Syst. Saf.* **206**, 107300 (2021).
5. Hersbach, H. *et al.* The ERA5 global reanalysis. *Q. J. R. Meteorol. Soc.* **146**, 1999–2049 (2020).
6. United Nations Framework Convention on Climate Change. GHG data from UNFCCC. (2023).
7. United Nations, D. of E. & Social Affairs, P. D. World Population Prospects 2015 Revision. (2015).
8. United Nations, D. of E. & Social Affairs, P. D. World Population Prospects 2022 Revision. (2022).
9. Columbia University, Center for International Earth Science Information Network, CIESIN. Gridded Population of the World, Version 4 (GPWv4): Population Density Adjusted to Match 2015 Revision UN WPP Country Totals, Revision 11. (2018) doi:10.7927/H4F47M65.
10. Kaza, S., Yao, L. C., Bhada-Tata, P. & Woerden, F. V. *What a Waste 2.0*. (The World Bank Group, 2018).
11. Esri, Maxar, Earthstar Geographics & Community, the G. U. ESRI World Imagery. (2022).